Computational Mechanics (2020) 66:723–743
https://doi.org/10.1007/s00466-020-01874-6

ORIGINAL PAPER

Finite deformation cohesive zone phase field model for crack propagation in multi-phase microstructures

Preetam Tarafder[1] · Saikat Dan[1] · Somnath Ghosh[2]

Received: 30 March 2020 / Accepted: 17 June 2020 / Published online: 7 July 2020

Abstract
This paper develops a unified phase field model for simulating finite deformation crack evolution and interfacial decohesion in multi-phase elastic materials. Crack propagation is formulated using a phase field model, in which the order parameter $s = 1$ corresponds to the crack topology. The phase field model at the interface is enhanced with cohesive zone characteristics through a cohesive potential function. The interface displacement discontinuities are regularized using an auxiliary interface phase field order parameter. The cohesive potential is associated with this interface phase field for delineating interfacial decohesion. The model is numerically implemented using a multi-pass staggered solver. Numerical examples involving different failure mechanisms are simulated for examining the performance of the proposed model. Different failure mechanisms such as interfacial debonding, crack kinking and propagation in the brittle matrix, and their interactions are captured by the model. Limited verification tests are conducted with analytical results.

Keywords Phase field model · Multi-phase materials · Crack evolution · Cohesive-zone interfacial decohesion · Finite deformation

1 Introduction

Composite materials are used in a variety of high performance applications, e.g. in the aerospace, automotive and energy industry, among others. Despite their enhanced thermo-mechanical properties, the presence of second-phase fibers or particulates in their microstructures often adversely affect their failure properties like toughness, ductility and fatigue life. Major failure modes in composite microstructures include second-phase inclusion (fiber or particulate) breakage, inclusion-matrix interfacial debonding and matrix cracking [79]. Damage often initiates with interfacial decohesion [13,31,62] or breakage of inclusions and subsequently evolves with matrix crack growth and bridging, leading to overall failure. Mechanisms like crack deflection, penetration, branching and arresting have also been observed to occur near the interfaces due to interactions with other cracks [39,45,46,55]. A robust modeling framework that accounts for the interfacial properties, as well as the interaction between interfacial debonding and evolving cracks in the inclusion and matrix phases of the microstructure is necessary for predicting failure in composite materials. While there have been developments in modeling microstructural failure in composite microstructures, there is a significant need for robust physics-based models.

A variety of approaches have been proposed for modeling crack propagation in heterogeneous microstructures. Some of them use linear elastic fracture mechanics (LEFM) to model material cracking. The extended FEM or XFEM [11,56], the cohesive zone models or CZM [58,65,87], the generalized finite element methods [10,26], and the discontinuous Galerkin approach [2,90] are among popular computational methods that introduce idealized surfaces for discrete crack representation. In many of these methods, the crack propagation-rate and direction are determined from stress intensity factors or global energy release-rate. Many of these models require modifications to the computational model, e.g. mesh adaptation, element deletion or explicit mesh separation, which are computationally inefficient especially when dealing with 3D non-planar cracks.

✉ Somnath Ghosh
sghosh20@jhu.edu

[1] Department of Civil Engineering, Johns Hopkins University, Baltimore, USA

[2] Departments of Civil, Mechanical and Material Science Engineering, Johns Hopkins University, 3400 N. Charles St., Baltimore, MD 21218, USA

Cohesive zone models or CZMs require cohesive elements embedded between adjacent finite elements along the projected crack path with special traction-separation constitutive relations [69]. They have been extensively used for modeling interfacial decohesion and crack propagation in [25,34,35,40,41]. However, major shortcomings arise with efficient handling of stress transfer [88], and with them requiring *a-priori* knowledge of 3D crack paths for inserting the traction-separation laws. The XFEM was originally developed in [11,14,56] to avert this *a-priori* crack-path estimation, as well as adaptive re-meshing with crack propagation. A cogent review is presented in [12]. It has been widely used for modeling failure in multi-phase materials e.g. in [18,71,83]. Although XFEM alleviates some of the limitations of CZMs, it suffers from shortcomings of appropriate augmentation functions for 3D crack tip fields especially in the presence of heterogeneities, as well as criteria to nucleate cracks. 3D level-set functions that are conventionally used in X-FEM to represent crack surface topology can be very difficult with heterogeneities of composite microstructures. Non-local methods like peridynamics [75,76] have been successfully proposed to model crack propagation predominantly in elastic media. However their use in modeling crack propagation in heterogeneous materials is quite limited.

Phase field (PF) models [5,19,21,24,52,74] have shown promise in overcoming many of the above difficulties and have received considerable attention from the fracture community in the recent years. This method is based on the regularization of a sharp crack surface through an auxiliary scalar field variable or order parameter $s \in [0, 1]$ to represent the crack topology. The sharp crack discontinuity is approximated by a smooth transition between the uncracked ($s = 0$) and fully-cracked ($s = 1$) material phases [19,36]. The evolution of s with deformation and loading naturally models the crack growth process. Because of its thermodynamically consistent framework [17,50,52], the phase field models are able to implicitly track complex crack mechanisms including crack nucleation, propagation and branching without the need to introduce any *a-priori* crack path or remeshing due to discontinuous fracture surfaces. Phase field approaches have been successfully used for a wide variety of fracture problems encompassing ductile fracture [6,22,54], dynamic fracture [16,33], fatigue [43,49], fracture with contact applications [37] as well as fracture in multi-physics scenarios [1,23,51,53,84]. PF modeling augmented with Global-Local approach has been implemented for anisotropic brittle fracture [64] and hydraulic fracture [4]. Recent works have also focused on the formulation of PF models using Virtual Element Method [3]. Coupled phase field and crystal plasticity FE models have been developed by the Ghosh group in [20,74,81] for predicting failure in polycrystalline materials. In [20,81] an adaptive wavelet-based hierarchical enrichment method has been developed to automatically provide high mesh density in the vicinity of high gradients in the phase field order parameter near the crack.

A majority of the phase field models have thus far been applied to homogeneous materials without interfaces belonging to heterogeneous phases. A few studies have been conducted in the recent years to account for interfacial damage. A phase field model for cohesive fracture has been developed in [82] that uses an auxiliary field to model displacement jump across interfaces. This formulation has however been shown to have instability issues in [47], due to to stress oscillations for unstructured meshes. To address the issue of stress oscillation and to enhance accuracy, a Bernstein Bzier discretization is used in [28] instead of conventional Lagrangian interpolation. In [73] a multi phase field model has been used to describe cracks in heterogeneous materials. The interfacial properties are accounted for through the grain boundary energy rather than the interface fracture toughness. A hybrid phase field model has been proposed in [30,66], where cracks in the individual phases are modeled by the phase field order parameter, while interfacial debonding is modeled by an order parameter dependent CZM. The model implements a simple linear tension cut-off CZM, as the dependency of CZMs on the order parameter may restrict the implementation of more commonly used CZMs [89]. Hence, this model is not suitable for most fracture problems. The phase field model in [60] accounts for complex interactions between inclusion and matrix cracks and interfacial failure. The displacement jump across interfaces is approximated as a smooth transitioning level-set function, and interfaces are regularized by an auxiliary order parameter. A similar approach has been adopted in [88] where the material properties are regularized using the auxiliary interface phase field to model progressive failure in multi-phase systems. A phase field model for interfacial damage has been introduced in [31], where the interface is distributed over a finite thickness and the effect of individual phases on interfacial crack propagation is compensated using an exaggeration function that depends on the fracture toughness ratio of the interface and individual phases. An extension to this model has been proposed in [32] to account for elastic heterogeneities.

This paper develops a unified fracture modeling framework for inclusion/matrix cracking and interfacial decohesion in elastic composite microstructures undergoing finite deformation. The framework is capable of modeling different microstructural damage mechanisms such as interfacial decohesion that has a defined crack path, and crack propagation in the matrix/inclusion phases for which the paths are not know *a-priori*. The formulation is based on a phase field model introduced in [74] for modeling crack propagation in anisotropic polycrystalline materials under finite strain conditions. The model inherently accounts for

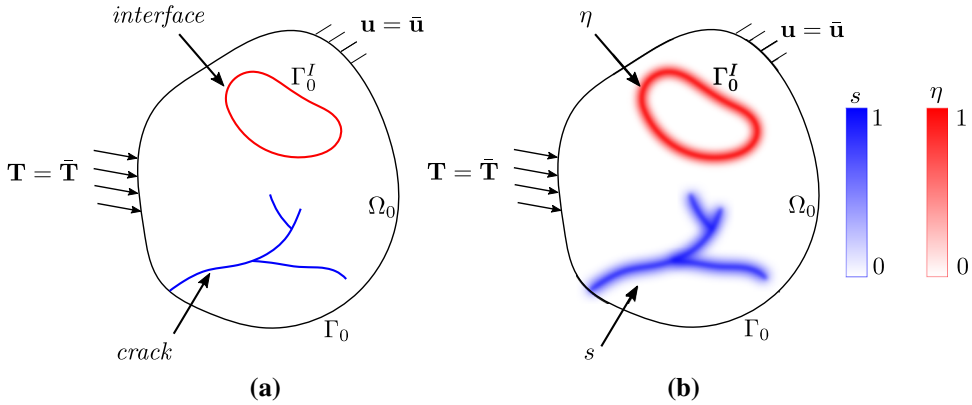

Fig. 1 Schematic diagram of a microstructural domain with interacting cracks and interfaces: **a** Discrete representation of the cracks and interfaces. **b** Regularized representation of the cracks and interfaces by scalar field order parameters s and η respectively

tension–compression asymmetry of the material response due to the presence of crack fields. This unified formulation follows that in [60,88], where an auxiliary non-evolving order parameter is introduced to describe interfaces in the microstructural domain. A schematic of cracking in the multi-phase microstructure is shown in Fig. 1. The model is also effectively able to predict competing mechanisms of crack deflection and penetration at the interfaces.

This paper begins with a brief discussion of the Helmholtz free energy density function for crack phase field problem in Sect. 2. Section 3 establishes the formulation for incorporating cohesive zone model-based interfacial damage in the phase field framework. The kinematics of discontinuous displacement fields and the regularization of interfaces are also discussed. In Sect. 4 the governing equations for the coupled displacement and phase field problem, along with viscous stabilization and the finite element weak forms with solution scheme are briefly discussed. 2D and 3D simulations are conducted in Sect. 5, followed by concluding remarks in Sect. 6.

2 Finite strain phase field model for crack propagation in homogeneous elastic materials

In the phase field formulation, the crack phase field and its gradient regularize the geometric features of the sharp crack topology. Crack evolution results from energy dissipation by releasing the stored energy following thermodynamic principles with the crack geometric function. This section summarizes a finite deformation Helmholtz free energy density function that has been derived in [74] for degrading anisotropic elastic materials, while exhibiting tension–compression asymmetry.

2.1 Phase field regularization of a discrete crack

In phase field formulation for fracture problems, a continuous order parameter $s \in [0, 1]$ is introduced to represent the regularized crack topology. $s = 0$ describes an intact material while $s = 1$ describes a completely cracked material. The order parameter s regularizes the discrete crack surface through a functional $\Gamma_{l_c}(s)$, which in 3D is given as:

$$\Gamma_{l_c}(s) = \int_{\Omega_0} \gamma_{l_c} \, \mathrm{d}\Omega_0 \tag{1}$$

$$\text{where} \quad \gamma_{l_c} = \frac{1}{2l_c}\left(s^2 + l_c^2 \nabla_{\mathbf{X}} s \cdot \nabla_{\mathbf{X}} s\right) \tag{2}$$

l_c is a length-scale parameter that controls the sharpness of the crack in the regularized representation and $\nabla_{\mathbf{X}}$ is the gradient operator in the reference configuration. For $l_c \to 0$ the functional $\Gamma_{l_c}(s)$ converges to the exact sharp crack geometry.

2.2 Helmholtz free energy density function for elastic materials with evolving cracks

The finite deformation fields and the crack phase field are coupled through a Helmholtz Free Energy Density (HFED) function in the reference configuration. For elastic materials, the HFED is assumed to be the sum of stored elastic energy density $\rho_0 \psi^e$ due to elastic stretching and the crack surface energy density $\rho_0 \psi^c$, written as:

$$\rho_0 \psi = \rho_0 \psi^e \left(\mathbf{E}^e, s\right) + \rho_0 \psi^c \left(s, \nabla_{\mathbf{X}} s\right) \tag{3}$$

where ρ_0 is the material density in the reference configuration. The first term on the RHS of Eq. (3)is the elastic energy density $\rho_0 \psi^e$, which is a function of the Green–Lagrange strain tensor $\mathbf{E}^e = \frac{1}{2}(\mathbf{F}^{eT}\mathbf{F}^e - \mathbf{I})$, expressed in terms of the elastic deformation gradient $\mathbf{F}^e$ and the identity tensor $\mathbf{I}$. To account for the degrading effect of crack evolution on the

stored elastic energy density, a phase field order parameter s dependent degrading Green–Lagrange elastic strain tensor $\tilde{\mathbf{E}}^e$ has been proposed in [74] for the coupled FE-phase field model. $\tilde{\mathbf{E}}^e$ represents tension–compression asymmetry of crack fields under finite strain conditions and is obtained from isochoric-volumetric decomposition of the elastic deformation gradient as:

$$\mathbf{F}^e = \mathbf{F}^e_{iso}\,\mathbf{F}^e_{vol} \tag{4}$$

where $\mathbf{F}^e_{iso} = (J^e)^{-\frac{1}{3}}\,\mathbf{F}^e$ and $\mathbf{F}^e_{vol} = (J^e)^{\frac{1}{3}}\,\mathbf{I}$ are the volumetric and isochoric parts of the elastic deformation gradient respectively, and $J^e = \det \mathbf{F}^e$ is the elastic Jacobian. The corresponding degrading elastic Green–Lagrange strain tensor is expressed as:

$$\tilde{\mathbf{E}}^e = g_1(J^e, s)\mathbf{E}^e_{vol} + g_2(s)\mathbf{E}^e \tag{5a}$$

$$\text{with}\quad g_1(J^e, s) = \mathcal{H}(1 - J^e)(1 - \kappa_s)s \quad \text{and}$$

$$g_2(s) = [1 - (1 - \kappa_s)s] \tag{5b}$$

Here $\mathbf{E}^e_{vol} = \frac{1}{2}(\mathbf{F}^{eT}_{vol}\mathbf{F}^e_{vol} - \mathbf{I})$ represents the volumetric part of the elastic strain tensor and $\mathcal{H}(\alpha)$ is the Heaviside step function. $\kappa_s \ll 1$ is a small positive number that is introduced to avoid singularity of the stiffness matrix for a fully degraded material. The formulation in Eq. (5a) preserves tension–compression asymmetry of the crack fields in finite deformation through the term $\mathcal{H}(1 - J^e)s$. $J^e > 1$ indicates a positive (tensile) volume change while $J^e < 1$ denotes a negative (compressive) volume change. For a positive volume change in Eq. (5a), both the isochoric and volumetric components of $\mathbf{E}^e$ are degraded with s. For a negative volume change, the volumetric part $\mathbf{E}^e_{vol}$ is added back to the second term in the equation, and hence the tension–compression asymmetry. The form of the stored elastic energy density derived in [74] is:

$$\rho_0\psi^e = \frac{1}{2}\tilde{\mathbf{E}}^e(s) : \mathbb{C}^e : \tilde{\mathbf{E}}^e(s) \tag{6}$$

where $\mathbb{C}^e$ is the anisotropic elastic stiffness that is independent of the evolving order parameter s. Tension–compression asymmetry has been accounted for in fracture models of isotropic materials in [7,15], where the strain energy is split into deviatoric and volumetric components. Such energy splitting is however difficult for anisotropic materials and cannot be used in the present context. Consequently, the tension–compression asymmetry consideration is accommodated in Eq. (5) by decomposing the Green–Lagrange strain tensor into volumetric and isochoric parts. This approach allows the use of this tension–compression asymmetry formulation for materials with any degree of anisotropy.

The second term on the RHS of Eq. (3) is the crack surface energy density $\rho_0\psi^c$ that is commonly expressed in terms of a Griffith type fracture energy per unit area $\mathcal{G}_c$ and the regularized crack surface density γ_{l_c} in Eq. (2), given as [50,52]:

$$\rho_0\psi^c = \mathcal{G}_c\gamma_{l_c} = \frac{\mathcal{G}_c}{2l_c}\left(s^2 + l_c^2\nabla_{\mathbf{X}}s\cdot\nabla_{\mathbf{X}}s\right) \tag{7}$$

$\rho_0\psi^c$ in the above equation has a quadratic dependence on the phase field order parameter s, which causes immediate material degradation with deformation. An alternate form of $\rho_0\psi^c$ with a linear dependence on s has been proposed in [44,53,72] as:

$$\rho_0\psi^c = 2w_c\left(s + \frac{l_c^2}{2}\nabla_{\mathbf{X}}s\cdot\nabla_{\mathbf{X}}s\right) \tag{8}$$

where w_c is the specific fracture energy per unit volume. This form provides a linear elastic phase prior to the onset of degradation. The form in Eq. (8) has been shown to be computationally expensive in [61]. It has also been shown in [74] that the evolution of the crack phase field occurs in a physically consistent manner for both the forms of $\rho_0\psi^c$. Moreover, while Eq. (7) yields instantaneous material degradation with straining, the damage accumulated at a small load is minimal and does not significantly influence the overall material response. Consequently, the crack surface energy density in Eq. (7) is adopted in this work. Simulations are conducted under isothermal conditions and the temperature evolution is not considered in Eq. (3).

3 Interfacial failure using cohesive zone phase field model for materials with inclusions

The phase field formulation for homogeneous materials in Sect. 2 is now extended to accommodate cohesive zone modeling of interfacial decohesion in heterogeneous materials containing multiple phases. The finite deformation, cohesive zone phase field formulation is described in the following subsections.

3.1 Finite deformation kinematic relations of interfacial decohesion

Consider a multi-phase domain $\Omega(\mathbf{x})$ with a boundary $\Gamma(\mathbf{x})$ that is undergoing finite deformation under external loading, where $\mathbf{x}$ corresponds to the current coordinates of a material point $\mathbf{X}$. Assume that the domain consists of n internal interfaces Γ^I_i, $i = 1, \ldots, n$, where the ith interface due to the disparate phases divides Ω into sub-domains Ω^+_i and Ω^-_i.

Let the reference (undeformed) configuration $\Omega_0(\mathbf{X})$ with a boundary $\Gamma_0(\mathbf{X})$, shown in Fig. 2. It corresponds to an inverse mapping $\mathbf{X} = \chi^{-1}(\mathbf{x})$, where $\mathbf{X}$ and χ are respectively the material coordinates and coordinate mapping function respectively. In the reference configuration, the n internal interfaces are represented as $\Gamma_{0i}^I, \quad i = 1, \ldots, n$, where the ith interface divides Ω_0 into sub-domains Ω_{0i}^+ and Ω_{0i}^-. For each interface Γ_{0i}^I, $\mathbf{N}_i^I$ represents the outward normal pointing towards Ω_{0i}^+.

Assume that with deformation, the interfaces undergo decohesion causing a discontinuity in the displacement field across the interfaces. Represented in the reference configuration, the total displacement field (corresponding to the current coordinates $\mathbf{x}$) can therefore be expressed as the additive decomposition of its continuous and discontinuous parts as [8,9,77]:

$$\mathbf{u}(\mathbf{X}) = \mathbf{x} - \mathbf{X} = \underbrace{\mathbf{u}^c(\mathbf{X})}_{\text{continuous}} + \underbrace{\sum_{i=1}^{n} [\![\mathbf{u}]\!]_i \mathcal{H}_{\Gamma_{0i}^I}(\mathbf{X})}_{\text{discontinuous}} \tag{9}$$

where $[\![\mathbf{u}]\!]_i$ denotes the jump in the displacement field $\mathbf{u}$ across the ith interface and $\mathcal{H}_{\Gamma_{0i}^I}(\mathbf{X})$ is the Heaviside step function given as:

$$\mathcal{H}_{\Gamma_{0i}^I}(\mathbf{X}) = \begin{cases} 1 & \text{for } \mathbf{X} \in \Omega_{0i}^+ \\ 0 & \text{for } \mathbf{X} \in \Omega_{0i}^- \end{cases} \tag{10}$$

The spatial coordinates of the material point $\mathbf{X}$ in Ω can be written as:

$$\mathbf{x} = \mathbf{X} + \mathbf{u}^c(\mathbf{X}) + \sum_{i=1}^{n} [\![\mathbf{u}]\!]_i \mathcal{H}_{\Gamma_{0i}^I}(\mathbf{X}) \tag{11}$$

The deformation gradient tensor is obtained as:

$$\mathbf{F} = \mathbf{I} + \nabla_{\mathbf{X}} \mathbf{u}^c + \sum_{i=1}^{n} [\![\mathbf{u}]\!]_i \otimes \mathbf{N}_i^I \delta_{\Gamma_{0i}^I} \tag{12}$$

where $\nabla_{\mathbf{X}}$ is the gradient operator in the reference configuration, $\delta_{\Gamma_{0i}^I}$ denotes the Dirac-delta function at Γ_{0i}^I and $\otimes$ indicates the tensor product. Following [8,57], the deformation tensor in Eq. (12) may be expressed with a multiplicative decomposition $\mathbf{F} = \mathbf{F}^e \mathbf{F}^d$, where

$$\mathbf{F}^e = \mathbf{I} + \nabla_{\mathbf{X}} \mathbf{u}^c \tag{13a}$$

$$\mathbf{F}^d = \mathbf{I} + \sum_{i=1}^{n} \mathbf{J}_i \otimes \mathbf{N}_i^I \delta_{\Gamma_{0i}^I} \tag{13b}$$

Here $\mathbf{F}^e$ is the deformation gradient component corresponding to the continuous part of the total displacement field and $\mathbf{F}^d$ is the deformation gradient component associated with the discontinuous part. In Eq. (13b) $\mathbf{J}_i$ is defined as a pull-back vector of the displacement jump $[\![\mathbf{u}]\!]_i$ in the intermediate configuration [8,57] as shown in Fig. 2. It is expressed as:

$$\mathbf{J}_i = \mathbf{F}^{e^{-1}} [\![\mathbf{u}]\!]_i \tag{14}$$

From Eq. (13b) it is seen that the multiplicative decomposition $\mathbf{F} = \mathbf{F}^e \mathbf{F}^d$ holds only for $\mathbf{X} \in \Gamma_{0i}^I$ and it reduces to $\mathbf{F} = \mathbf{F}^e$ for $\mathbf{X} \in \Omega_{0i}^{\pm}$.

3.2 Phase field regularization of sharp interfaces

Implementation of the cohesive zone models for interfacial decohesion requires a-priori knowledge of the interfacial topologies in the domain. To facilitate this implementation, a regularized representation of the pre-damaged interfaces in the undeformed configuration is introduced through a functional Γ_{l_I} as discussed in [60]. Analogous to the crack phase field in Eq. (2), the auxiliary interface phase field order parameter $\eta \in [0, 1]$ in this representation manifests the known interface topology in the reference configuration Ω_0. The order parameter η is solved from the governing equation [60,88]:

$$\eta - l_I^2 \nabla_{\mathbf{X}} \cdot \nabla_{\mathbf{X}} \eta = 0 \qquad \text{in} \quad \Omega_0 \tag{15}$$

subject to Dirichlet boundary condition $\eta = 1$ on the internal interfaces Γ_{0i}^I for all $i = 1, \ldots, n$. The Neumann boundary condition on the domain boundary Γ_0 is assumed to be zero. l_I is a length-scale parameter that determines the spread of the regularized interface. In the limit, $l_I \to 0$ restores the exact geometry of the sharp interface. Since the initial interface topology does not evolve with deformation, the interface phase field order parameter η is solved only once prior to the deformation process. With a known η field, the functional Γ_{l_I} used for regularizing sharp interfaces can be expressed as:

$$\Gamma_{l_I}(\eta) = \int_{\Omega_0} \gamma_{l_I} \, \mathrm{d}\Omega_0, \quad \text{where} \tag{16a}$$

$$\gamma_{l_I} = \frac{1}{2 l_I} \left(\eta^2 + l_I^2 \nabla_{\mathbf{X}} \eta \cdot \nabla_{\mathbf{X}} \eta \right) \tag{16b}$$

3.3 Regularized displacement discontinuity at interfaces

Following [60,85], the displacement jump $[\![\mathbf{u}]\!]_i$ at interfaces shown in Fig. 3 is approximated as:

$$[\![\mathbf{u}]\!]_i \approx \mathbf{u}^c(\mathbf{X}_i^+) - \mathbf{u}^c(\mathbf{X}_i^-) \tag{17}$$

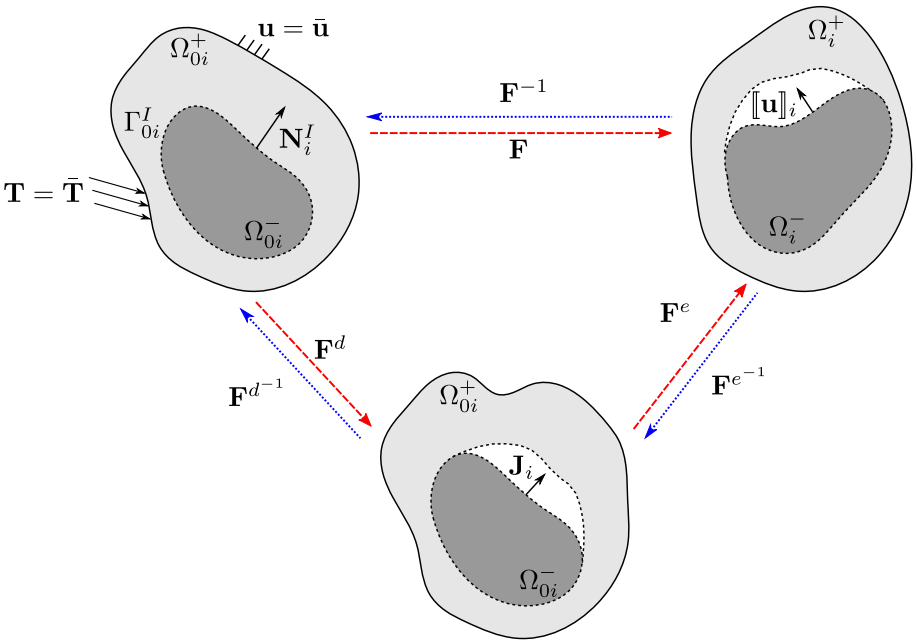

Fig. 2 Reference, intermediate and current configurations of a heterogeneous domain undergoing finite deformation. The intermediate configuration is obtained through an inverse mapping of the current configuration by the tensor $\mathbf{F}^{e^{-1}}$. It delineates a mapping of the displacement jump $[\![\mathbf{u}]\!]_i$ to a vector $\mathbf{J}_i$

where $\mathbf{X}_i^+ = \mathbf{X} + \frac{h}{2}\mathbf{N}_i^I$ and $\mathbf{X}_i^- = \mathbf{X} - \frac{h}{2}\mathbf{N}_i^I$ are two material points on either side of the interface Γ_{0i}^I. The displacement field at $\mathbf{X}_i^+$ and $\mathbf{X}_i^-$ in Eq. (17) can be written from the first order terms in the Taylor expansion (see Fig. 3) as:

$$\mathbf{u}^c\left(\mathbf{X} + \frac{h}{2}\mathbf{N}_i^I\right) = \mathbf{u}^c(\mathbf{X}) + \frac{h}{2}\nabla_{\mathbf{X}}\mathbf{u}^c(\mathbf{X})\mathbf{N}_i^I \tag{18a}$$

$$\mathbf{u}^c\left(\mathbf{X} - \frac{h}{2}\mathbf{N}_i^I\right) = \mathbf{u}^c(\mathbf{X}) - \frac{h}{2}\nabla_{\mathbf{X}}\mathbf{u}^c(\mathbf{X})\mathbf{N}_i^I \tag{18b}$$

where h is a very small scalar displacement jump regularization parameter and $\mathbf{N}_i^I$ is the normal to the interface Γ_{0i}^I. Substituting Eq. (18) in Eq. (17), the displacement jump can be approximated by a smooth transition function as:

$$[\![\mathbf{u}]\!]_i \approx \mathbf{w}_i = h\nabla_{\mathbf{X}}\mathbf{u}^c\mathbf{N}_i^I \tag{19}$$

Here $\mathbf{w}_i$ corresponds to a smooth displacement jump function. Unlike [60], where the interface normal has been evaluated by using level-set functions, $\mathbf{N}_i^I$ at the internal interfaces are evaluated directly in this work from the interface phase field order parameter η as:

$$\mathbf{N}_i^I = \frac{\nabla_{\mathbf{X}}\eta}{\|\nabla_{\mathbf{X}}\eta\|}\Big|_{\mathbf{X}\in\Gamma_{0i}^I} \tag{20}$$

where $\|\cdot\|$ corresponds to the L_2 norm of a vector. Substituting Eqs. (13a) and (19) in Eq. (14), the regularized displacement jump in the intermediate configuration can be approximated as:

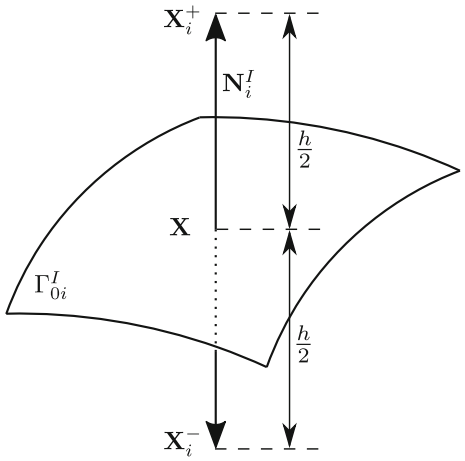

Fig. 3 Schematic of displacement jump regularization across an interface

$$\mathbf{J}_i = h(\mathbf{I} - \mathbf{F}^{e^{-1}})\mathbf{N}_i^I = h(\mathbf{I} - \mathbf{F}^{e^{-1}})\frac{\nabla_{\mathbf{X}}\eta}{\|\nabla_{\mathbf{X}}\eta\|}\Big|_{\mathbf{X}\in\Gamma_{0i}^I} \tag{21}$$

3.4 Phase field modeling of interfacial decohesion

The following ansatz is adopted for incorporating interfacial decohesion in the phase field model. The deformation gradient tensor $\mathbf{F}^d$, corresponding to the discontinuous component of the displacement field, is expressed in terms of the regularized interface density function γ_{l_l} in Eq. (16) as:

$$\mathbf{F}^d = \mathbf{I} + \sum_{i=1}^{n} \mathbf{J}_i \otimes \mathbf{N}_i^I \gamma_{l_l} \tag{22}$$

As shown in "Appendix A", the function γ_{l_I} preserves the properties of Dirac-delta function $\delta_{\Gamma_{0i}^I}$. Substituting Eq. (21) in Eq. (22) yields the continuous component of the deformation gradient as:

$$\mathbf{F}^e = (\mathbf{F} + \mathbf{\Lambda})(\mathbf{I} + \mathbf{\Lambda})^{-1} \tag{23}$$

where $\mathbf{\Lambda} = \sum_{i=1}^{n} h\gamma_{l_I} \mathbf{N}_i^I \otimes \mathbf{N}_i^I$. In the numerical implementation of the finite deformation algorithm, the elastic component $\mathbf{F}^e$ is first computed in a given increment with the total deformation gradient tensor $\mathbf{F}$ using Eq. (23), and subsequently $\tilde{\mathbf{E}}^e$ is computed using Eq. (5a).

3.5 Cohesive zone model-based helmholtz free energy density function

To account for the additional energy contribution due to the discontinuous displacement field at the internal interfaces, the HFED function in Eq. (3) is augmented with an additional energy contribution, written as [85]:

$$\rho_0\psi = \rho_0\psi^e\left(\tilde{\mathbf{E}}^e\right) + (1-\eta)^2\rho_0\psi^c\left(s, \nabla_{\mathbf{X}} s\right) + \sum_{i=1}^{n} \rho_0\psi_i^I\left(\mathbf{J}_i, \gamma_{l_I}\right) \tag{24}$$

A potential-based cohesive zone model e.g. [59,70,86], in which traction-separation relationships across fracture surfaces are obtained from a potential function, is adopted in this study. Consequently, the term $\rho_0\psi_i^I\left(\mathbf{J}, \gamma_{l_I}\right)$ is the energy density that accounts for decohesion at the ith internal interface and is expressed as:

$$\rho_0\psi_i^I\left(\mathbf{J}_i, \gamma_{l_I}\right) = \phi_i(\Delta_{Ni}, \Delta_{Ti})\gamma_{l_I} \tag{25}$$

Here $\phi_i(\Delta_{Ni}, \Delta_{Ti})$ is the cohesive zone potential function, which depends on the normal and tangential components of $\mathbf{J}_i$ denoted by Δ_{Ni} and Δ_{Ti} respectively. These components of the displacement jump in the intermediate configuration are expressed as:

$$\Delta_{Ni} = \mathbf{J}_i \cdot \mathbf{N}_i^I \quad \text{and} \quad \Delta_{Ti} = \|\mathbf{J}_i - \mathbf{J}_i \cdot \mathbf{N}_i^I\| \tag{26}$$

The factor $(1-\eta)^2$ in Eq. (24) and the function γ_{l_I} in Eq. (25) respectively ensure that the cohesive zone model is activated only at the interfaces, and the constitutive behavior is governed by the cohesive zone potential function throughout the regularized interfacial zone. Away from the interfacial zone, the contribution from cohesive zone potential to the HFED reduces with diminishing influence of the interface phase field, and increasing dominance of the crack phase field in individual phases. In the limiting case, i.e. $\eta \to 0$ and $\gamma_{l_I} \to 0$, the modified HFED in Eq. (24) reduces to the HFED in homogeneous materials, discussed in Sect. 2.

3.5.1 Potential function in cohesive zone model

The cohesive zone potential function used in this work is based on the unified potential-based PPR model, proposed in [70] and discussed in [68]. The formulation in this paper is equally applicable to any other potential-based cohesive zone model, such as those in [59,86]. The PPR potential incorporates different fracture energies for each mode along with other physical parameters such as cohesive strength, initial slope and shape parameters for cohesive interactions and is suitable for modeling arbitrary mixed mode fracture and is expressed as:

$$\begin{aligned}\phi(\Delta_N, \Delta_T) &= \min(\phi_n, \phi_t) \\ &+ \left[\Gamma_n\left(1 - \frac{\Delta_N}{\delta_n}\right)^{\alpha}\left(\frac{m}{\alpha} + \frac{\Delta_N}{\delta_n}\right)^{m} + \langle\phi_n - \phi_t\rangle\right] \\ &\times \left[\Gamma_t\left(1 - \frac{|\Delta_T|}{\delta_t}\right)^{\beta}\left(\frac{n}{\beta} + \frac{|\Delta_T|}{\delta_t}\right)^{n} + \langle\phi_t - \phi_n\rangle\right]\end{aligned} \tag{27}$$

where ϕ_n and ϕ_t are the energies for mode I and Mode II fracture and Γ_n and Γ_t are energy constants in the PPR potential. Δ_N and Δ_T are the normal and tangential components of the displacement jump. In a standard cohesive zone modeling framework, these components are determined from the nodal displacements of the cohesive elements faces, as discussed in [80]. However in the cohesive zone phase field framework, they are computed using Eq. (26). δ_n and δ_t are the final crack openings representing complete failure in the normal and tangential directions. They are determined from the condition that the areas under the traction-separation curves are equal to the mode I and mode II fracture energies respectively. α and β represent the shape parameters, while the initial slopes are controlled by the non-dimensional exponents m and n. $\langle\cdot\rangle$ denotes the Macaulay bracket.

The normal and tangential traction forces are determined from the derivatives of the potential function ϕ with respect to the normal and tangential displacement jump fields respectively. This yields:

$$\begin{aligned}T_n(\Delta_N, \Delta_T) &= \frac{\Gamma_n}{\delta_n}\left[m\left(1 - \frac{\Delta_N}{\delta_n}\right)^{\alpha}\left(\frac{m}{\alpha} + \frac{\Delta_N}{\delta_n}\right)^{m-1}\right. \\ &\left. - \alpha\left(1 - \frac{\Delta_N}{\delta_n}\right)^{\alpha-1}\left(\frac{m}{\alpha} + \frac{\Delta_N}{\delta_n}\right)^{m}\right] \\ &\times \left[\Gamma_t\left(1 - \frac{|\Delta_T|}{\delta_t}\right)^{\beta}\left(\frac{n}{\beta} + \frac{|\Delta_T|}{\delta_t}\right)^{n} + \langle\phi_t - \phi_n\rangle\right]\end{aligned} \tag{28a}$$

$$T_t(\Delta_N, \Delta_T) = \frac{\Gamma_t}{\delta_t}\left[n\left(1 - \frac{|\Delta_T|}{\delta_t}\right)^{\beta}\left(\frac{n}{\beta} + \frac{|\Delta_T|}{\delta_t}\right)^{n-1} - \beta\left(1 - \frac{|\Delta_T|}{\delta_t}\right)^{\beta-1}\left(\frac{n}{\beta} + \frac{|\Delta_T|}{\delta_t}\right)^{n}\right] \times \left[\Gamma_n\left(1 - \frac{\Delta_N}{\delta_n}\right)^{\alpha}\left(\frac{m}{\alpha} + \frac{\Delta_N}{\delta_n}\right)^{m} + \langle \phi_n - \phi_t \rangle\right]\frac{\Delta_T}{|\Delta_T|} \tag{28b}$$

The maximum normal and tangential strength σ_{max} and τ_{max} are given by the traction values at critical separation δ_{nc} and δ_{tc} respectively, i.e. $T_n(\delta_{nc}, 0) = \sigma_{max}$ and $T_t(0, \delta_{tc}) = \tau_{max}$. The initial slope indicators λ_n and λ_t are given by the ratio of the critical separation to the final crack opening width.

4 Governing equations for the coupled deformation and phase field crack problem

The governing equations for the coupled finite deformation and phase field crack problem in a Lagrangian description are summarized in this section. In the reference configuration Ω_0 with boundary Γ_0, the principle of virtual power for the coupled problem is given as [20,74]:

$$\int_{\Omega_0} \mathbf{P} : \delta\dot{\mathbf{F}}\, \mathrm{d}\Omega_0 + \int_{\Omega_0} \boldsymbol{\xi}_0 \cdot \nabla_{\mathbf{X}} \delta\dot{s}\, \mathrm{d}\Omega_0 + \int_{\Omega_0} \pi_0\, \delta\dot{s}\, \mathrm{d}\Omega_0 = \int_{\Gamma_{0T}} \mathbf{T} \cdot \delta\dot{\mathbf{u}}\, \mathrm{d}\Gamma_{0T} + \int_{\Omega_0} \mathbf{B} \cdot \delta\dot{\mathbf{u}}\, \mathrm{d}\Omega_0 + \int_{\Gamma_{0\lambda}} \lambda_0\, \delta\dot{s}\, \mathrm{d}\Gamma_{0\lambda} + \int_{\Omega_0} \zeta_0\, \delta\dot{s}\, \mathrm{d}\Omega_0 \tag{29}$$

where $\mathbf{P}$ is the first Piola–Kirchhoff stress tensor and $\mathbf{F}$ is the total deformation gradient, $\mathbf{T}$ is the applied traction loading on Γ_{0T} and $\mathbf{B}$ is the body force per unit volume. For the phase field problem, π_0 and $\boldsymbol{\xi}_0$ are the internal microforces and power-conjugate to the rate of the phase field order parameter $\dot{s}$ and its gradient $\nabla_{\mathbf{X}}\dot{s}$ respectively.

Applying the divergence theorem to terms containing gradients in Eq. (29), setting $\delta\dot{s} = 0$ and $\delta\mathbf{u} = 0$ on Γ_{0u}, and considering that the integral should hold for any arbitrary volume Ω_0 yields the governing equation for the quasi-static displacement field as:

$$\nabla_{\mathbf{X}} \cdot \mathbf{P} + \mathbf{B} = 0 \qquad \text{in} \quad \Omega_0 \tag{30}$$

subject to Dirichlet boundary condition $\mathbf{u} = \bar{\mathbf{u}}$ on Γ_{0u} and Neumann boundary condition $\mathbf{T} = \mathbf{PN} = \bar{\mathbf{T}}$ on Γ_{0T}. Analogously, setting $\delta\dot{\mathbf{u}} = 0$ with $\delta s = 0$ on Γ_{0s} and considering that the integral should be valid for any arbitrary volume Ω_0 the governing equation for the evolving crack phase field is given as:

$$\nabla_{\mathbf{X}} \cdot \boldsymbol{\xi}_0 - \pi_0 + \zeta_0 = 0 \qquad \text{in} \quad \Omega_0 \tag{31}$$

subject to Dirichlet boundary condition $s = \bar{s}$ on Γ_{0s}. The external traction loading $\lambda_0 = \rho_0 \dfrac{\partial\psi}{\partial \nabla_{\mathbf{X}} s} \cdot \mathbf{N}$ for the order parameter is assumed to be zero.

Constitutive relations for the coupled problem can be established through the first and second law of thermodynamics and are expressed as:

$$\mathbf{P} = \rho_0 \frac{\partial\psi}{\partial \mathbf{F}} \tag{32a}$$

$$\boldsymbol{\xi}_0 = \rho_0 \frac{\partial\psi}{\partial \nabla_{\mathbf{X}} s} \quad \text{and} \quad \pi_0 = \rho_0 \frac{\partial\psi}{\partial s} \tag{32b}$$

Incremental solutions to the governing Eqs. (30) and (31) at time $t + \Delta t$ are obtained from known displacement and crack phase field values at time t, by solving their coupled weak forms using the backward Euler method. To avert solving the coupled problem with large degrees of freedom, a multi-pass staggered solution scheme is adopted. In this algorithm, one field is kept frozen while the other field is being iteratively solved using a Newton–Raphson type solver.

For problems involving material degradation due to fracture, instabilities can occur in the constitutive models depending on the model geometry and constitutive parameters. This can cause the iterative solver to face convergence issues as observed and reported in [27,29,42,48,74,78]. In [29] it is shown that the fracture process leads to excessive energy release, which can be equilibrated by incorporating dynamical effects into the formulation. However, in the absence of the kinetic energy as in the case of quasi-static formulation, the excessive energy cannot be balanced and leads to non-equilibrium states. In this case, the iterative solvers are unable to find feasible solutions and therefore lack convergence. Such issues have been discussed in [27,42], where the excess energy is identified as the cause of convergence issues. Arc-length formulations have been proposed in [48,78] for phase field modeling of brittle fracture. In [74] a 1-D problem has been studied to demonstrate that crack evolution causes an excess energy in the system for which no static equilibrium path exists. Static and quasi-static numerical solvers are not able to find a feasible solution and leads to convergence issues. A viscous stabilization method has been adopted in [74] as an effective way to circumvent these issues. This is discussed in Sect. 4.1. More details about the weak form of the governing equations and the solution scheme are described in Sect. 4.3.

4.1 Viscous stabilization to resolve convergence issues in the coupled model

Following [74], a viscous stabilization is adopted in this work for overcoming the aforementioned convergence issues. To attenuate the instability with fracture evolution, the governing equations are augmented with artificial viscosity that allows the system to dissipate excess energy and thus achieve a convergent solution without resorting to any dynamic formulation. The artificial viscosity augmented equations are given as [74]:

$$\nabla_{\mathbf{X}} \cdot \mathbf{P} + \mathbf{B} = \beta_{gu}\dot{\mathbf{u}} \quad \text{in} \quad \Omega_0 \tag{33a}$$

$$\nabla_{\mathbf{X}} \cdot \rho_0 \frac{\partial \psi}{\partial \nabla_{\mathbf{X}} s} - \rho_0 \frac{\partial \psi}{\partial s} = \beta_{ls}\dot{s} \quad \text{in} \quad \Omega_0 \tag{33b}$$

in which $\beta_{gu} = \beta_{gu_0} s$ and β_{ls} are non-negative viscous parameters for the displacement and phase field respectively.

In addition, the first Piola–Kirchhoff stress is also stabilized using another non-negative viscous parameter β_{lu}. The stabilized first Piola–Kirchhoff stress tensor is given as:

$$\mathbf{P} = \rho_0 \frac{\partial \psi}{\partial \mathbf{F}} + \beta_{lu}\mathbf{F}\dot{\mathbf{E}} \tag{34}$$

where $\mathbf{E}$ is the total Green–Lagrange strain tensor. The analytical derivation of $\mathbf{P}$ is given in "Appendix B".

4.2 Enforcing crack irreversibility

Substituting Eqs. (3) and (7) into Eq. (33b), yields:

$$\beta_{ls}\dot{s} = \rho_0 \frac{\partial \psi^e}{\partial s} - \frac{\mathcal{G}_c}{l_c}\left(s - l_c^2 \nabla_{\mathbf{X}} \cdot \nabla_{\mathbf{X}} s\right) \tag{35}$$

where the term $\rho_0 \dfrac{\partial \psi^e}{\partial s}$ denotes a mechanical driving force f_{mech}. From Eq. (35) it is seen that for a given f_{mech}, the condition $\dot{s} \geq 0$ always holds. In the incremental solution process, for a given time step $[t, t+\Delta t]$ replacing f_{mech} with $\max_{[t,t+\Delta t]} (f_{mech})$ in Eq. (35) ensures irreversibility of crack phase field.

4.3 Weak forms of the governing equations and solution scheme

The method of weighted residual is applied to Eqs. (33a) and (33b) to obtain the weak forms of the coupled displacement and crack phase field problem. The weak form of the displacement field problem is given as:

$$\int_{\Omega_0} \left(\mathbf{P} : \nabla_{\mathbf{X}} \delta\mathbf{u} - \mathbf{B} \cdot \delta\mathbf{u} + \beta_{gu}\dot{\mathbf{u}} \cdot \delta\mathbf{u}\right) \mathrm{d}\Omega_0 - \int_{\Gamma_{0T}} \mathbf{T} \cdot \delta\mathbf{u} \, \mathrm{d}\Gamma_{0T} = 0 \tag{36}$$

and the weak form of the phase field problem is given as:

$$\int_{\Omega_0} \rho_0 \frac{\partial \psi}{\partial \nabla_{\mathbf{X}} s} \cdot \nabla_{\mathbf{X}} \delta s \, \mathrm{d}\Omega_0 + \int_{\Omega_0} \left(\rho_0 \frac{\partial \psi}{\partial s} + \beta_{ls}\dot{s}\right) \delta s \, \mathrm{d}\Omega_0 = 0 \tag{37}$$

As mentioned in Sect. 4, an incremental solution process is adopted for numerical integration of the coupled, nonlinear finite deformation and phase field problem. With known displacement field $\mathbf{u}$, crack phase field s and internal state variables at time t, the weak forms in Eqs. (36) and (37) are solved for $\mathbf{u}$ and s at time $t + \Delta t$ using a multi-pass staggered solution scheme. The variables η, s and $\mathbf{u}$ are passed from one field to the other and are termed as inter-field information (IFI). The solution scheme iterates between the displacement field problem and phase field problem until both the fields converge. A flowchart detailing the multi-pass staggered solution scheme is shown in Fig. 4.

5 Numerical results

To explore the capability of the coupled deformation and crack phase field models proposed in Sect. 3, 2D and 3D composite problems with different interface configurations are simulated in this section. In the first example, a double cantilever beam with a weak interface is simulated to compare fracture predictions by the finite and small deformation formulations. Next, an example of a single fiber-matrix composite microstructure, subjected to transverse tensile loading, is solved. This example demonstrates the necessity of including an explicit interface with appropriate interfacial properties, as it ensures the correct sequence of fracture mechanisms in such two-phase material problems. The next problem considered is for a heterogeneous microstructure with multiple fibers randomly embedded in a matrix. This problem manifests a complex crack path leading to the complete failure of the microstructure.

Following analysis of the fiber-matrix composite microstructures, an example of a bi-material system with inclined interface is examined. The problem of a crack impinging on an interface is studied and the model is compared against analytical results obtained from linear elastic fracture mechanics (LEFM). A matrix with an embedded particle is studied next. Damage characteristics, e.g. crack nucleation and propagation, are predicted using the current formulation using a 3D model.

Conventional 3-noded constant-strain triangle and 4-noded constant-strain tetrahedral elements are used for FE

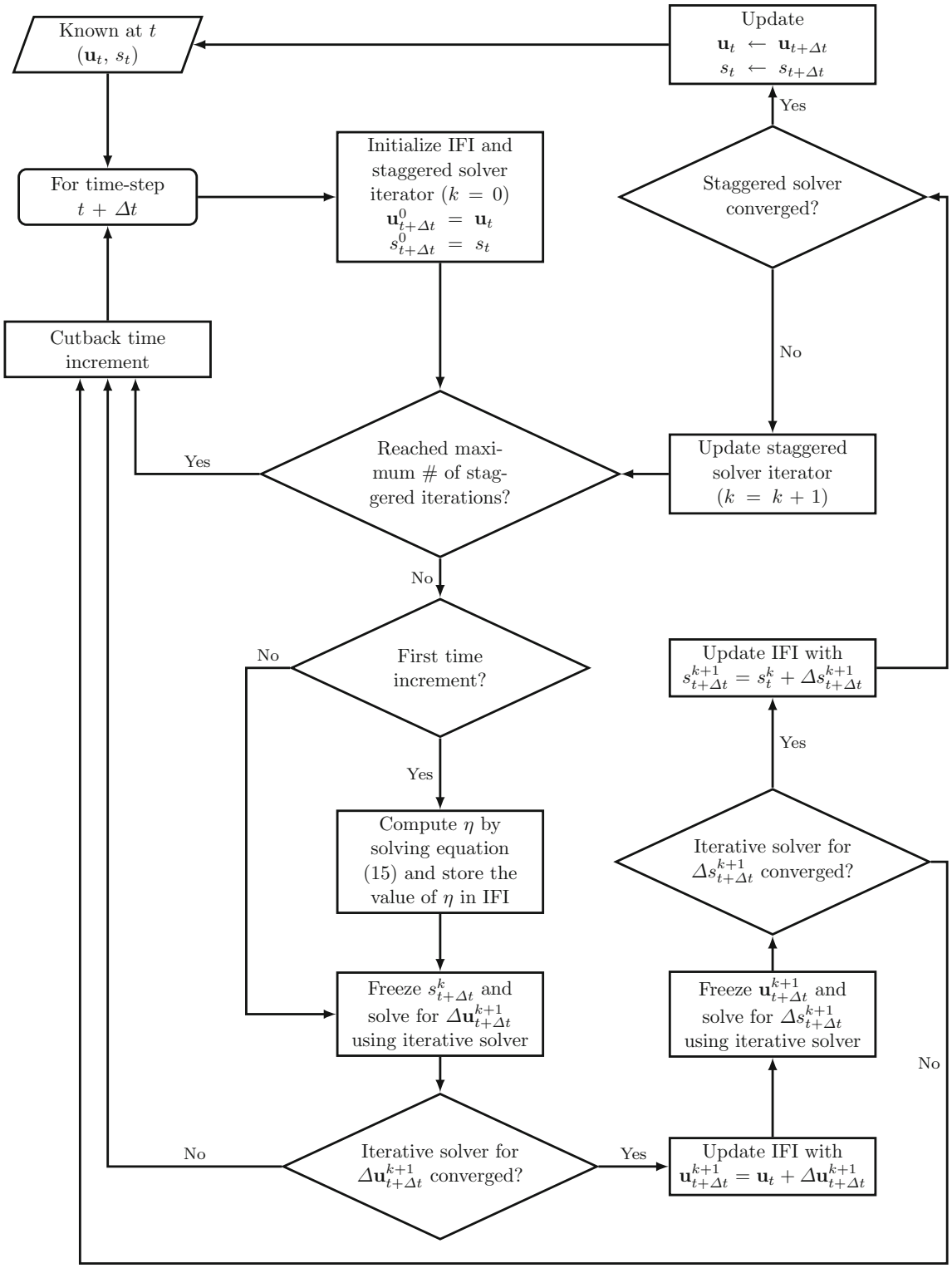

Fig. 4 Flowchart for multi-pass staggered solver for the coupled displacement field and crack phase field problem

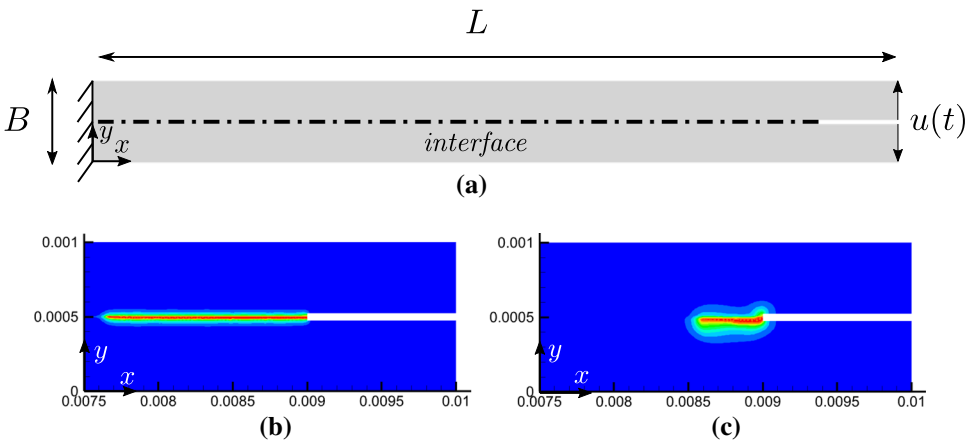

Fig. 5 **a** Schematic diagram of the DCB with a weak interface; the crack profile in the DCB for **b** finite deformation and **c** small deformation kinematics at $u = 0.16$ mm

modeling of the 2D and 3D problems respectively. Following discussions in [52], the mesh is chosen such that the effective element size is half of the crack phase field regularization length scale parameter l_c. Also, according to parametric studies conducted in [60], the displacement jump regularization parameter h is taken to be approximately equal to the effective element size. The interface phase field regularization length scale parameter l_I is considered to be same as l_c [60,88]. For all the simulations, the values of shape parameters α and β in the PPR potential are fixed at 2.0. The artificial viscosity parameters are taken to be $\beta_{lu} = 10^4 \text{Pa} \cdot \text{s}$ and $\beta_{ls} = 10 \text{Pa} \cdot \text{s}$ for the 2D examples, whereas for 3D problems the values are chosen to be $\beta_{lu} = 10^8 \text{Pa} \cdot \text{s}$ and $\beta_{ls} = 10^2 \text{Pa} \cdot \text{s}$. The values of β_{gu} and κ_s is set to zero. It is important that the viscosity parameters are carefully chosen such that the mechanical response is not dominated by these parameters [74].

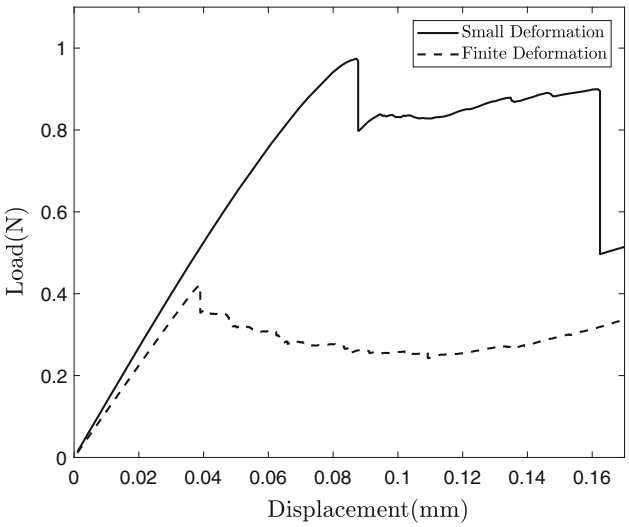

Fig. 6 Load-displacement response plot for the DCB

5.1 A double cantilever beam with weak interface

This example, involving a double cantilever beam (DCB), is solved to compare the effect of finite and small deformation kinematics on fracture characteristics. This problem is bending dominated, where larger flexural strains lead to additional bending stresses. A slender DCB with a weak interface is modeled as shown in Fig. 5a. The length L and thickness B of the beam are 10 mm and 1 mm respectively. The beam consists of an initial crack of length is 1 mm. The left edge of the beam at $x = 0$ mm is fixed in both the x and y directions. An equal and opposite uniform displacement $u(t) = 10^{-3}t$ mm is applied respectively on the upper and lower end of the right edge of the beam at $x = 10$ mm. The mechanical properties are obtained from [60] as: Young's modulus $E = 1$ GPa and Poisson's ratio $\nu = 0.3$. The critical energy rate is $\mathcal{G}_c = 100$ N/m. Only the normal traction component is considered for the interface. The interfacial properties are taken to be: $\phi_n = 10$ N/m, $\sigma_{max} = 1$ MPa and $\lambda_n = 0.015$. The viscosity parameters are set to zero. The length scale parameter l_c is chosen to be 0.025 mm, and correspondingly, a minimum mesh size of 0.0125 mm is taken at the interface.

The results of the DCB problem are compared for both finite and small deformation kinematics. For small deformation, the stored elastic energy density is given in "Appendix C". For the finite deformation problem, larger strains at the crack tip results in a longer crack with a more compliant response. For the small deformation problem, spurious stresses occur at the crack tip with much less crack growth for the same prescribed loading. Contour plots of the crack profile are depicted in Fig. 5b, c. The load displacement response plotted in Fig. 6 shows a significantly stiffer response with large load drops for the small strain problem. These differences allude to the use of large strains or rotations for certain problems with evolving fracture.

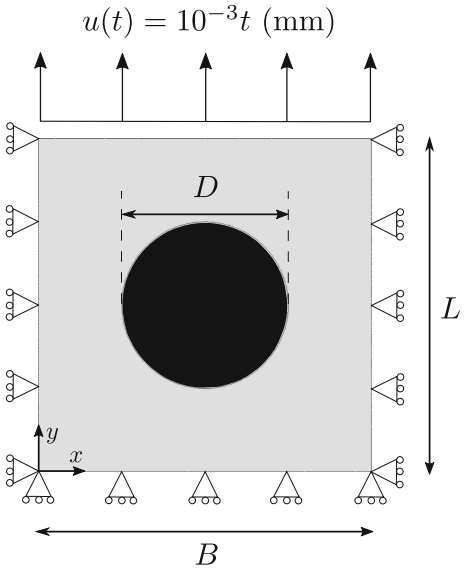

Fig. 7 Single fiber-matrix composite microstructure subjected to transverse tensile loading

5.2 Composite microstructure with a single fiber in the matrix

A microstructure consisting of a cylindrical hard fiber embedded in a square soft matrix is modeled as shown in Fig. 7. The dimensions of the microstructure is taken to be $L = B = 1$ mm with the fiber diameter $D = 0.5$ mm. The mechanical boundary conditions are as follows:
The lower edge $y = 0$ mm is restricted to move in the y-direction and a prescribed displacement field is applied on the upper edge $y = 1$ mm. The x-direction on both lower and upper edges are free. The remaining two edges i.e. $x = 0$ mm and $x = 1$ mm are restricted in the x-direction and free to move in the y-direction. Both the fiber and matrix materials are isotropic. The mechanical properties are taken from [88] and are given as:
For the matrix: Young's modulus $E_m = 4$ GPa, Poisson's ratio $\nu_m = 0.4$ and critical energy release rate $\mathcal{G}_c^m = 250$ N/m.
For the fiber: Young's modulus $E_f = 40$ GPa, Poisson's ratio $\nu_f = 0.33$ and critical energy release rate $\mathcal{G}_c^f = 400$ N/m. For simplicity, only the normal traction component of the interfacial cohesive potential accounted for in this example. The critical energy release rate ϕ_n in mode I is taken as 50 N/m and the cohesive strength σ_{max} is 10 MPa. The initial slope indicator λ_n is 0.2.

The length scale parameter is chosen to be 0.0075 mm for this problem. Therefore, a minimum mesh size of 0.00375 mm is considered near the interface, as well as in the region where a matrix crack is expected to propagate. Different stages of crack propagation are illustrated in Fig. 8. Two symmetric cracks nucleate from the upper and lower side of the interface. This crack nucleation is attributed to debonding of the fiber-matrix interface. Debonding occurs till a half-debonding angle of $\approx 72^o$ is achieved. This half-debonding angle is consistent with the $60^o - 70^o$ range reported in the boundary-element based micromechanical model in [67]. On further increasing the applied load, the crack on the upper side of the interface kinks into the matrix and initiates the process of matrix cracking, while that on the lower side is arrested. These observations are in good agreement with results reported in [38,63], where the crack profile is obtained using a discontinuous approach with cohesive elements. The load-displacement response curve is plotted in Fig. 9. The first drop in the load carrying capacity can be attributed to fiber-matrix debonding at the interface and the second drop in the curve is due to the matrix cracking.

The micromechanical problem in Fig. 7 is also solved by considering a coherent fiber-matrix interface using the formulation in Sect. 2 without the cohesive zone phase field model. The corresponding crack profile is shown in Fig. 10. From this example, it is obvious that the formulation without accounting for the interfacial damage predicts crack profiles that do not include interfacial decohesion. The differences in the crack profiles of Figs. 8 and 10 highlight the necessity of incorporating the interfacial properties, e.g. cohesive zone model in the interfacial phase field formulation.

5.3 Composite microstructure with randomly distributed fibers

This example models a composite microstructure consisting of multiple fibers randomly distributed in a relatively compliant matrix. Complex crack patterns are expected to evolve for this microstructure due to the interaction between interfacial debonds and nucleated cracks in the matrix. The geometry of the microstructure is illustrated in Fig. 11, which has a size of $L = B = 1$ mm. The fiber volume fraction of the two-dimensional computational domain is 13% with the fiber diameter being $D = 0.025$ mm for all fibers. The boundary conditions and the properties of the matrix, fibers and the cohesive interfaces are the same as for the single-fiber microstructure example in Sect. 5.2. The length scale parameter is chosen as 0.004 . Since the distribution of the fibers are random and the cracks can initiate and propagate at multiple locations, a uniform fine mesh with element size of 0.002 mm is adopted.

The evolving crack profile is shown in Fig. 12. It is observed that the debonding initiates and propagates at the fiber-matrix interfaces, which is followed by crack propagation into the matrix. This series of successive (sometimes simultaneous) debonding and matrix cracks leads to a complex array of cracks in the microstructure. However, with increase in loading, the cracks coalesce into a single dominant crack path that results in complete loss of stiffness of

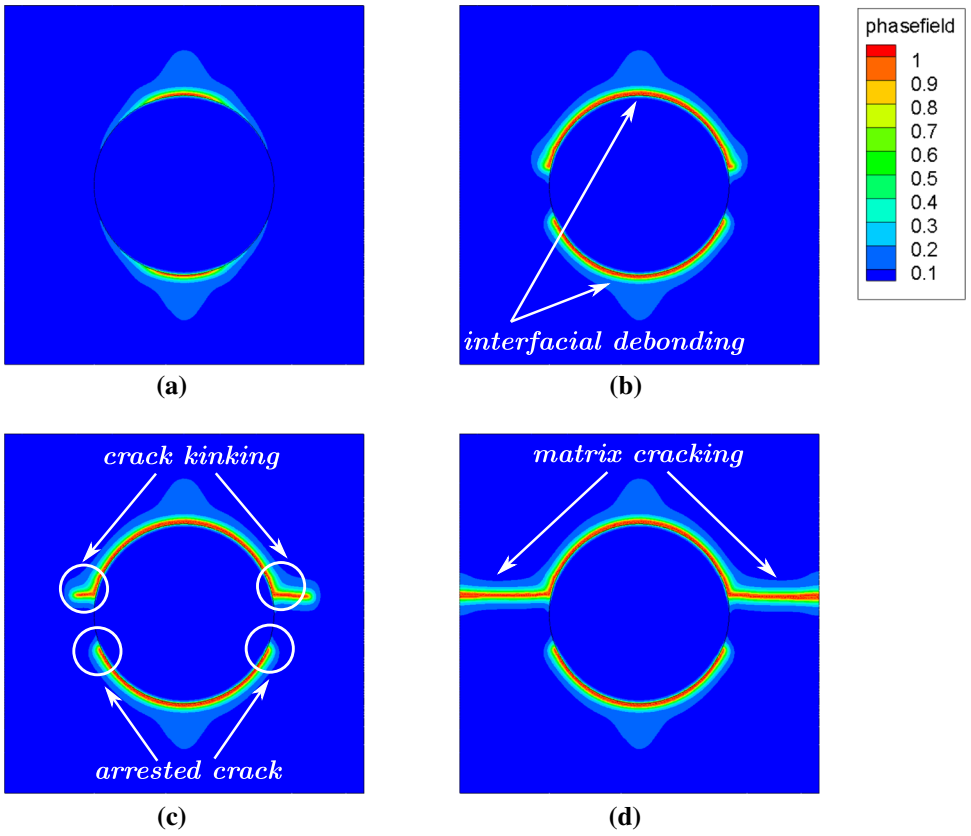

Fig. 8 Different stages of crack evolution in the single fiber-matrix composite microstructure at: **a** $t = 13.2702$ s, **b** $t = 14.9343$ s, **c** $t = 14.9445$ s and **d** $t = 14.9540$ s

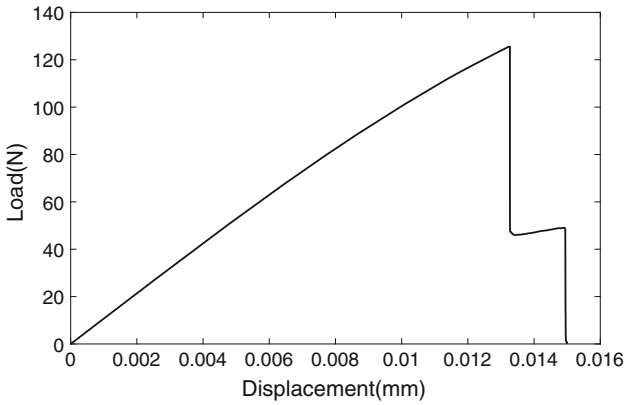

Fig. 9 Load-displacement curve for single fiber-matrix microstructure

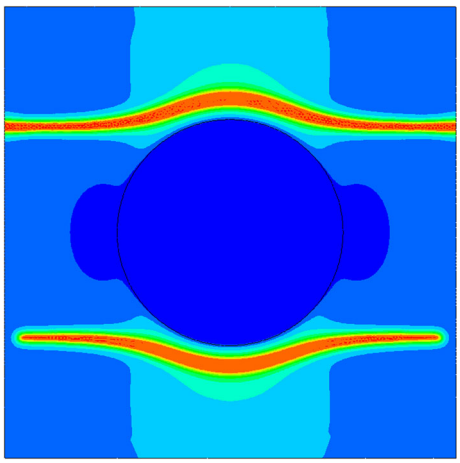

Fig. 10 Crack profile for single fiber-matrix microstructure without accounting for interfacial properties

the microstructure. This example further demonstrates that the formulation can capture complex mechanisms like interactions among multiple cracks and transition of cracks from interfacial debonding into matrix cracking.

5.4 Crack impinging on an inclined interface

This problem elucidates the competition between penetration and deflection of a crack impinging on an interface. It has been analytically investigated in [55] using LEFM and in [31, 66,89] using different variations of the phase field approach.

According to LEFM, the ratio of the energy release-rate $\mathcal{G}_d$ for a deflecting crack to that of a penetrating crack $\mathcal{G}_p$, is a function of the inclination angle θ_{int}. This ratio can be expressed as [55]:

$$\frac{\mathcal{G}_d}{\mathcal{G}_p} = \frac{1}{16}\left\{\left[3\cos\left(\frac{\theta_{int}}{2}\right) + \cos\left(\frac{3}{2}\theta_{int}\right)\right]^2\right.$$

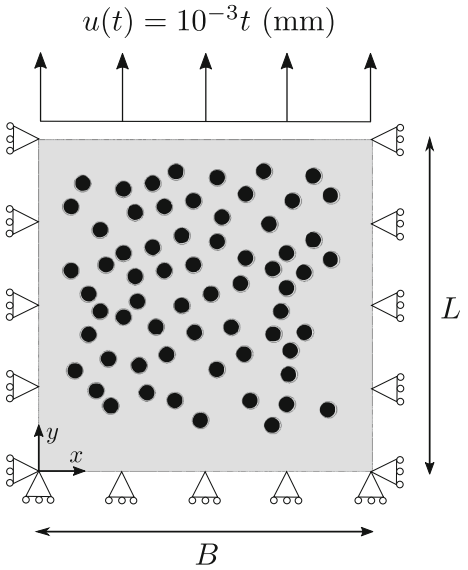

Fig. 11 Composite microstructure with multiple fibers randomly distributed in the matrix subjected to tensile loading

$$+\left[\sin\left(\frac{\theta_{int}}{2}\right)+\sin\left(\frac{3}{2}\theta_{int}\right)\right]^2\Bigg\} \tag{38}$$

Additionally, the criteria for crack deflection along the interface is given by:

$$\frac{\mathcal{G}_{int}}{\mathcal{G}_{bulk}} < \frac{\mathcal{G}_d}{\mathcal{G}_p} \tag{39}$$

where $\frac{\mathcal{G}_{int}}{\mathcal{G}_{bulk}}$ is the ratio of the fracture toughness of the interface to that of the matrix material. When this criteria is not met, the crack penetrates into the matrix. The plot separating the two possible cases of deflection and penetration is shown in Fig. 13.

The computational domain of a bi-material specimen with an oblique cohesive interface and a initial crack is shown in Fig. 14. The dimensions of the computational specimen are $L = B = 1$ mm. The length of the initial crack is taken to be $L/2 = 0.5$ mm. The specimen is subjected to uniform displacement loading on both the upper and lower edges i.e. at $y = 0$ mm and $y = 1$ mm. The material is isotropic and its mechanical properties are given as: Young's modulus $E = 210$ GPa and Poisson's ratio $\nu = 0.3$. These properties have been used for a similar numerical example without interface in [74]. For the interface, the mode I and mode II critical energy rates are assumed to be equal, i.e. $\phi_n = \phi_t = \mathcal{G}_{int}$, and the cohesive strengths σ_{max} and τ_{max} are both assumed to be 170 MPa. The initial slope indicators for both the normal

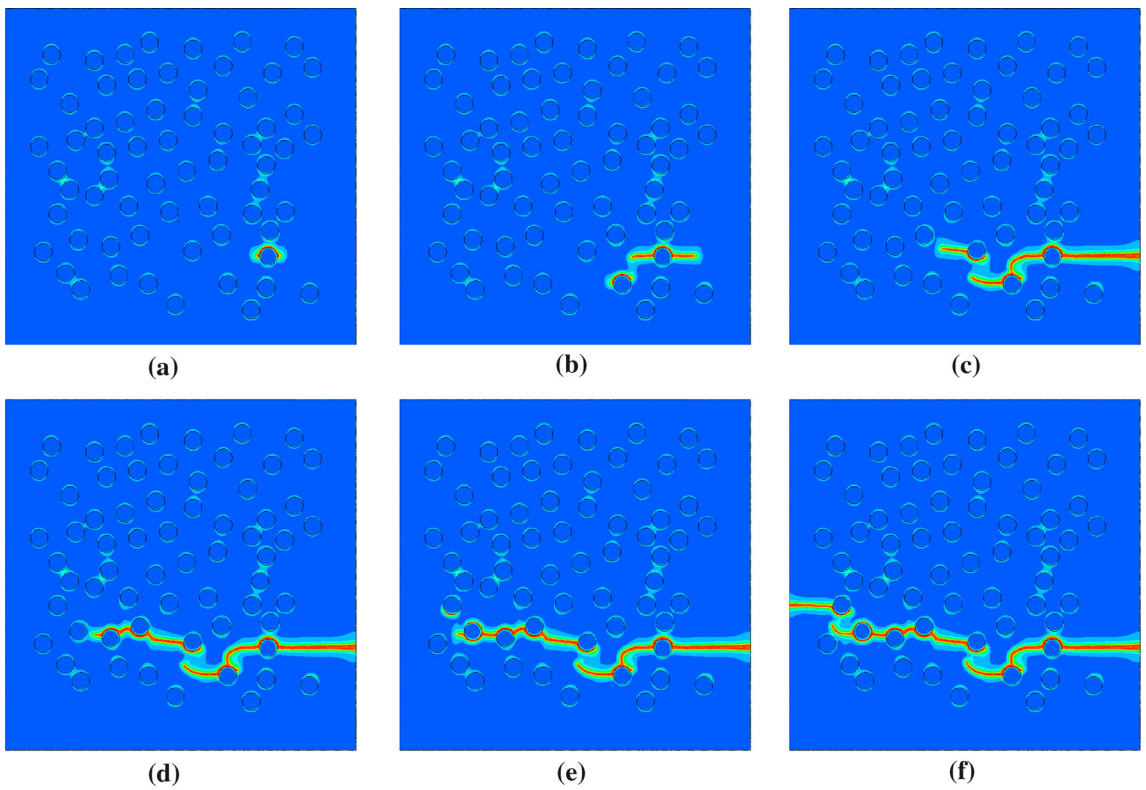

Fig. 12 Crack profile evolution in microstructure with randomly distributed multiple fibers at: **a** $t = 15.1882$ s, **b** $t = 15.1902$ s, **c** $t = 15.1939$ s, **d** $t = 15.1962$ s, **e** $t = 15.1982$ s, and **f** $t = 15.5002$ s

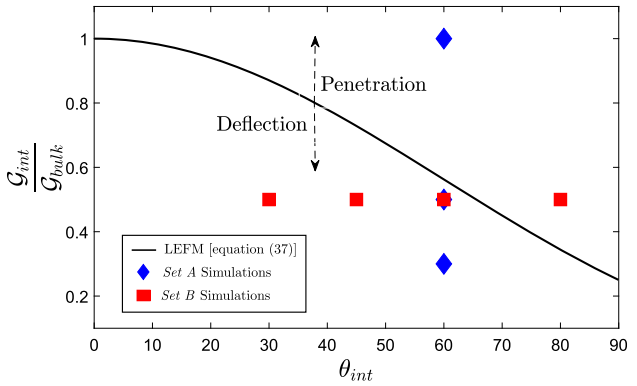

Fig. 13 The ratio of the fracture toughness ratio $\frac{\mathcal{G}_{int}}{\mathcal{G}_{bulk}}$ as a function of the interface inclination angle θ_{int} for two sets (A and B) of simulation conditions. The deflection-penetration curve is generated by LEFM [55]. The blue diamond markers represent the transition from deflecting crack to penetrating crack with increasing the fracture toughness ratio, while the red square markers depict the same transition with increasing inclination angle

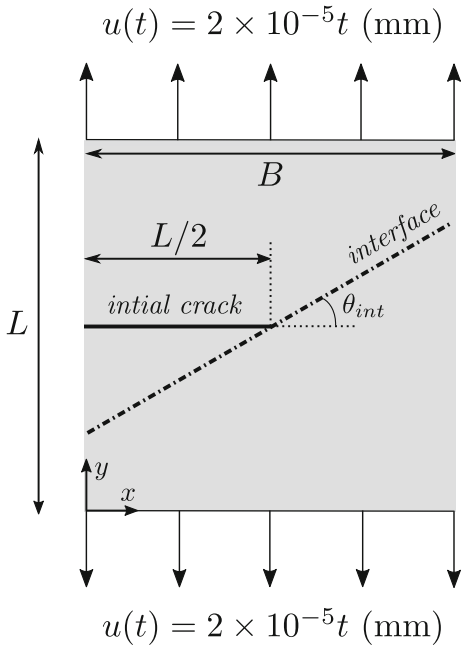

Fig. 14 Schematic of a bi-material specimen with an initial crack impinging on an inclined cohesive interface

and tangential separation are chosen to be $\lambda_n = \lambda_t = 0.015$. The length scale parameter is chosen to be 0.005 mm. Thus a fine mesh of element size 0.0025 mm is used to model the interface and the initial crack. The initial crack is modeled by a crack phase field value of ($s = 1$) assigned to nodes on it.

Two sets of simulations are performed for this example. In the first set (*Set A*) , the inclination of the interface is kept fixed at 60° and the ratio $\frac{\mathcal{G}_{int}}{\mathcal{G}_{bulk}}$ is varied. For the second set (*Set B*), the inclination angles are varied while keeping the ratio $\frac{\mathcal{G}_{int}}{\mathcal{G}_{bulk}}$ fixed at 0.5. The predicted crack profiles for the simulation *Set A* and *Set B* are shown in Figs. 15 and 16 respectively.

As depicted in Fig. 13, for the simulation *Set A*, the crack profile is expected to change from a deflecting crack to a penetrating crack with increase in the fracture toughness ratio $\frac{\mathcal{G}_{int}}{\mathcal{G}_{bulk}}$. This trend is clearly predicted by the proposed computational model as shown in Fig. 15, where the length of the crack path following the interface before penetrating into the matrix material reduces with increasing fracture toughness ratio $\frac{\mathcal{G}_{int}}{\mathcal{G}_{bulk}}$. Similarly for the simulations in *Set B*, the crack profile is expected to transition from deflection to penetration with increasing interface inclination angle. This transition is also captured well by the model as observed from the contour plots in Fig. 16. For $\theta_{int} = 30^o$ and 45^o, the crack fully deflects and no penetration takes place. For $\theta_{int} = 60^o$ the crack is initially deflected and then it penetrates into the matrix. No deflection occurs for $\theta_{int} = 80^o$, which is consistent with the analytical results from LEFM.

5.5 3D composite microstructure with hard particle embedded in a soft matrix

A 3D composite microstructure consisting of a hard spherical particle embedded in a soft matrix and subjected to tensile loading, is modeled as shown in Fig. 17. The microstructure is cubic with dimensions $10\,\mu m \times 10\,\mu m \times 10\,\mu m$, while the particle has a diameter of $5\,\mu m$. A prescribed displacement of $u(t) = 3 \times 10^{-3}\, t$ (μm) is applied in the y-direction on the xz plane with $y = 10\,\mu m$. The xz plane with $y = 0$ is restricted to move in the y-direction. Boundary conditions are applied to restrict any rigid body motion by restricting displacements in the x and z-directions along the lines $y = 0$ and $z = 0$ respectively. The matrix is epoxy with a bulk modulus $\kappa = 4.3$ GPa and a shear modulus $G = 3.5$ GPa. The particle is transversely isotropic with the plane of isotropy being perpendicular to y-axis. Mechanical properties of the particle are taken to be that of PZT-5H, given in Table 1.

In Table 1 E_x and E_y are the Young's modulus in x and y-directions respectively, G_{xy} is the shear modulus in the xy plane, and ν_{xy} and ν_{xz} represent the Poisson's ratio in the xy and xz planes respectively. $G_{xz} = \frac{E_x}{2(1+\nu_{xz})}$ is the shear modulus in the xz plane. Interfacial properties include the mode I and mode II fracture toughnesses ϕ_n=10 N/m and ϕ_t=40 N/m respectively, and the cohesive strengths σ_{max}=170 MPa and τ_{max}=120 MPa respectively. The initial slope indicators λ_n and λ_t are both equal to 0.015.

Figure 18 shows the evolved crack phase field order parameter s. The crack nucleates at the interface and then

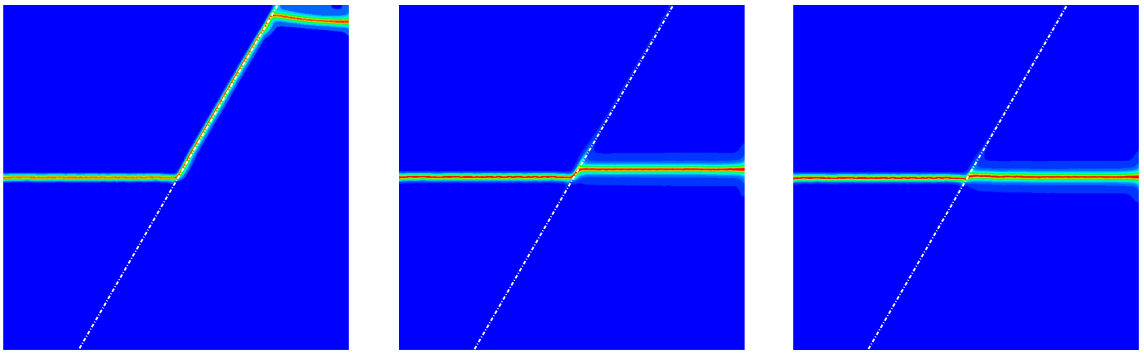

(a) $\frac{\mathcal{G}_{int}}{\mathcal{G}_{bulk}} = 0.3$ **(b)** $\frac{\mathcal{G}_{int}}{\mathcal{G}_{bulk}} = 0.5$ **(c)** $\frac{\mathcal{G}_{int}}{\mathcal{G}_{bulk}} = 1$

Fig. 15 Contour plots for the simulation set (*Set A*) depicting the crack path for different values of interface to matrix fracture toughness ratio $\frac{\mathcal{G}_{int}}{\mathcal{G}_{bulk}}$

Fig. 16 Contour plots for the simulation set (*Set B*) depicting the crack path for different values of interface inclination angle θ_{int}

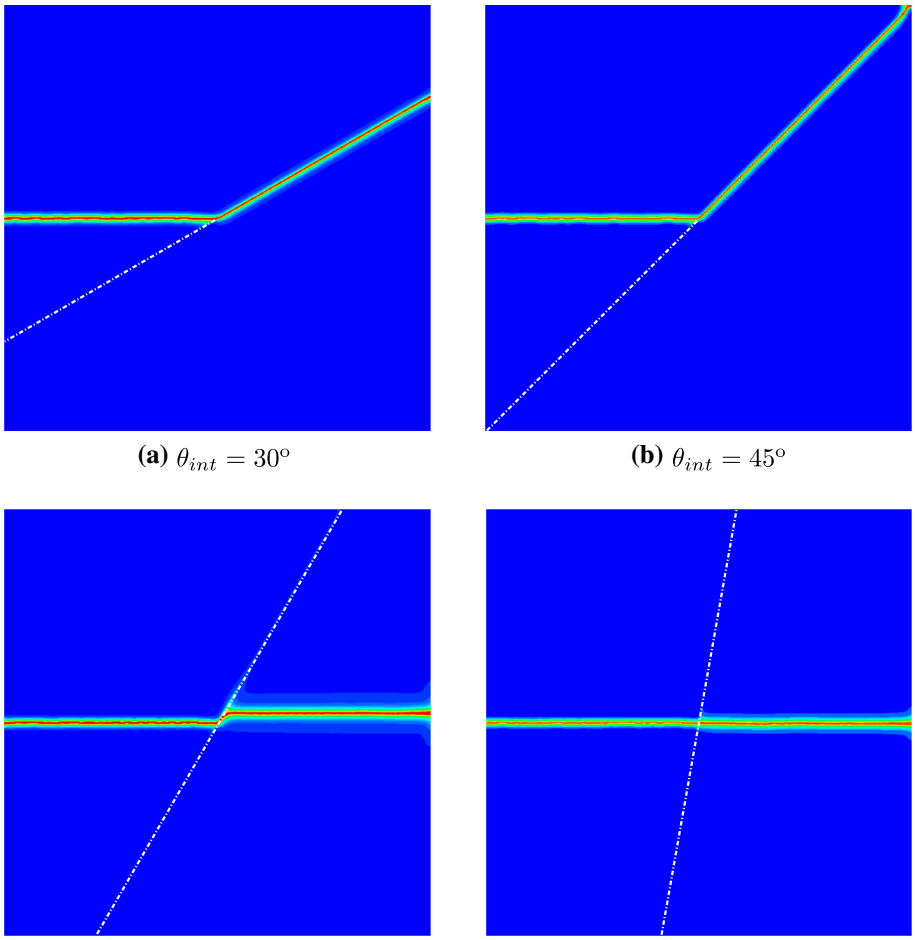

(a) $\theta_{int} = 30^{\circ}$ **(b)** $\theta_{int} = 45^{\circ}$

(c) $\theta_{int} = 60^{\circ}$ **(d)** $\theta_{int} = 80^{\circ}$

propagates into the matrix. Since the embedded particle is hard and has a higher critical energy release rate, the crack goes around the particle and does not penetrate. Debonding occurs until a critical kinking angle value is reached, after which the crack penetrates and starts propagating into the matrix until complete failure. It is also seen that the debonding, followed by matrix cracking, occurs only on one side of the particle. The crack propagation is axisymmetric about the loading axis. The load-displacement response is shown in Fig. 19. The initial snap-back is due to the interface decohesion between the particle and the matrix. This is followed by the growth of interface decohesion where the load increases

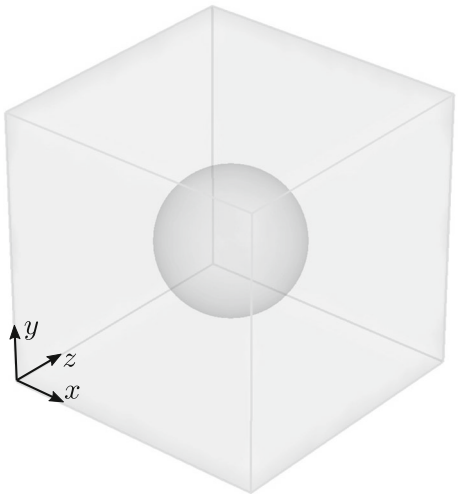

Fig. 17 3D composite microstructure consisting of a hard spherical particle embedded in a soft matrix

Table 1 Elastic properties of embedded particle

E_x (GPa)	E_y (GPa)	G_{xy} (GPa)	ν_{xy}	ν_{xz}
60	48.2	23	0.41	0.3

with the displacement. Finally, the crack kinks into the matrix and results in the complete loss of load carrying capacity.

6 Concluding remarks

This paper develops a finite deformation phase field model for multi-phase composite materials that can simultaneously predict cracking in individual phases as well as interfacial decohesion. The phase field model at the interface is enhanced with cohesive zone characteristics through a cohesive potential function to delineate the failure process at interfaces. The interface displacement discontinuities, corresponding to debonding, are regularized using an auxiliary interface phase field order parameter. The cohesive potential is associated with this interface phase field for delineating interfacial decohesion. A multi-pass staggered nonlinear finite element solver is employed to solve for the coupled set of governing differential equations for the displacement and crack phase field, resulting from the Helmholtz free energy density (HFED) function.

Several numerical examples involving interfacial decohesion and matrix cracking are conducted to assess the capabilities of the proposed model. The double cantilever beam problem elucidates the significant differences in finite deformation and small deformation solutions for fracture problems. The single fiber-matrix composite example shows good agreement with experimental observations. Different stages of failure processes are accurately captured by the model. They include cohesive debonding that initiates at the interface and grows along the interface till a critical debonding angle is reached, before penetrating into the matrix leading to complete failure. The example of the randomly dispersed multiple fibers in a composite microstructure system demonstrates a complex interacting crack growth process leading to a dominant single crack that fails the microstructure. Another benchmark problem simulated by the model explores competing phenomena of deflection and penetration of a crack that is impinging at an inclined interface. Results of the simulation compare well with trends predicted by LEFM. In the final example, a 3D microstructure consisting of a hard spherical particle embedded in a soft matrix under uni-axial tensile loading is analyzed. The simulation demonstrates the inception of interfacial decohesion that evolves into a 3D crack percolating the microstructure. Thus, the numerical examples solved highlight different aspects of the proposed model. A challenging issue with the phase field methods is however the enormous number of elements required to resolve the regularization length scale parameters. This problem can be significantly mitigated by the wavelet-adapted hierarchical mesh refinement techniques proposed in [20,81]. Moreover, This will be implemented in subsequent publications.

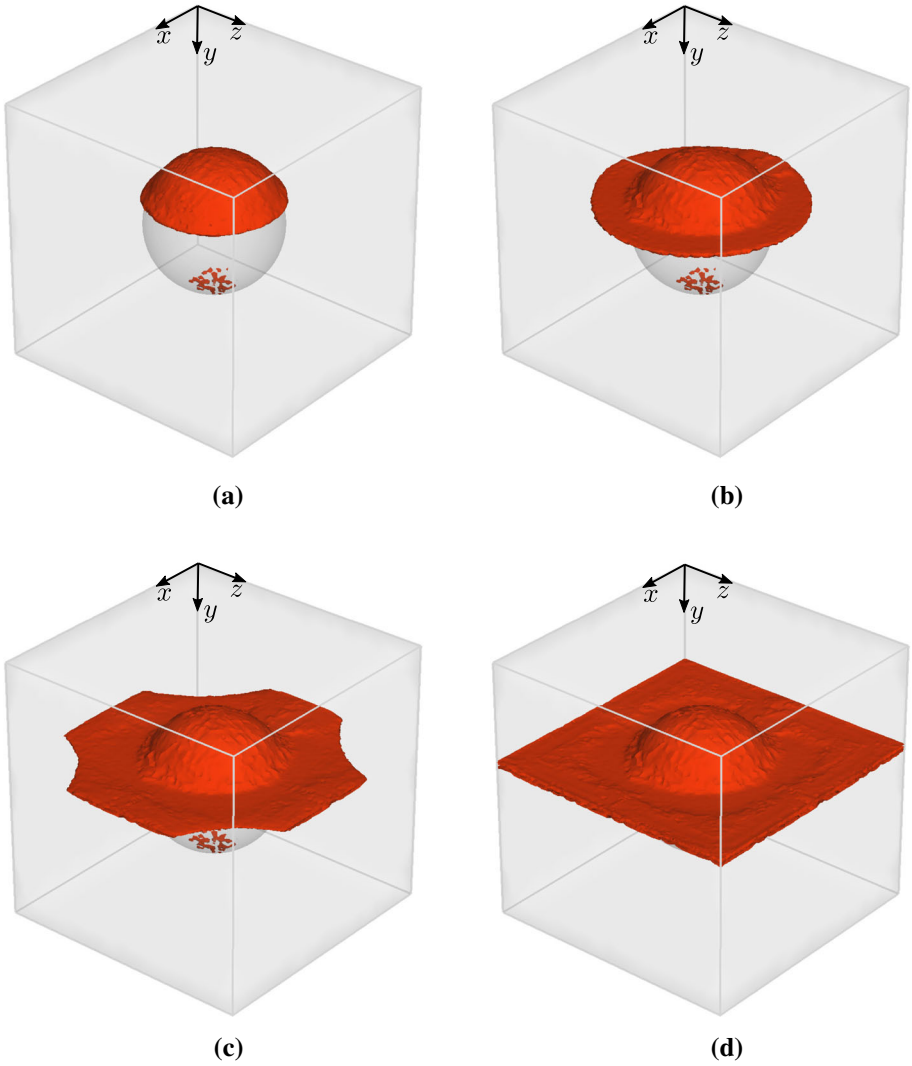

Fig. 18 Crack profile in the 3D microstructure at: **a** $t = 142.61$ s, **b** $t = 170.94$ s, **c** $t = 171.69$ s **d** $t = 172.39$ s. Only the order parameter field $0.95 \leq s \leq 1$ is visualized

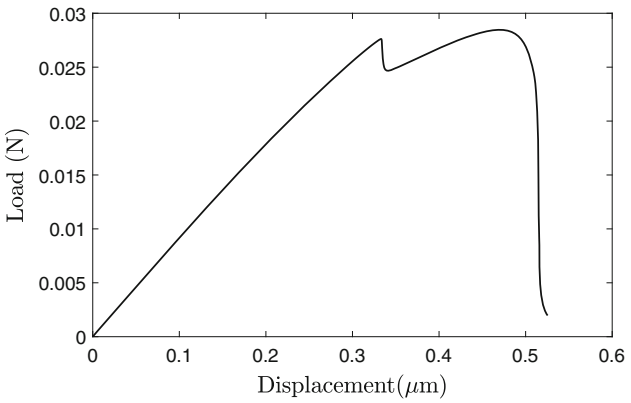

Fig. 19 Load-displacement response curve for the 3D microstructure

Acknowledgements This work has been sponsored by a Grant from the Mechanics of Multifunctional Materials & Microsystems Program of the Air Force Office of Scientific Research, through Grant No. FA9550-18-1-0536. The program director of this Grant is Dr. B.-L. (Les) Lee. The authors gratefully acknowledge the support of this work. Computational support for this work provided by the Johns Hopkins Homewood High Performance Compute Cluster (HHPC) and Maryland Advanced Research Computing Center (MARCC) is also gratefully acknowledged.

Appendix A: Equivalence of dirac delta function and regularized interface density

The equivalence of the regularized interface density γ_{l_I} and the Dirac delta function $\delta_{\Gamma_{0i}^I}$ is established in this appendix. The solution to Eq. (15) in 1D in the domain with boundary conditions $\eta(0) = 1$ and $\eta(\pm\infty) = 0$ is given by [88]:

$$\eta(x) = e^{-\frac{|x|}{l_I}} \tag{40}$$

Using Eqs. (40) and (16) gives the regularized interface density function in 1D as:

$$\gamma_{l_I} = \frac{1}{l_I} e^{-\frac{2|x|}{l_I}} \tag{41}$$

Integrating Eq. (41) within $(-\infty, \infty)$ gives:

$$\int_{-\infty}^{\infty} \gamma_{l_I} dx = \frac{2}{l_I} \int_0^{\infty} e^{-\frac{2x}{l_I}} dx = -e^{-\frac{2x}{l_I}}\Big|_0^{\infty} = 1 \tag{42}$$

which is also a property of Dirac-delta function. Thus, γ_{l_I} preserves the property of Dirac-delta function.

Appendix B: Derivation of first Piola–Kirchhoff stress tensor

The first Piola–Kirchhoff stress tensor is derived analytically in this appendix. The following tensor derivatives are used in the rest of the appendix:

$$\left(\frac{\partial \tilde{\mathbf{E}}^e}{\partial \mathbf{F}^e}\right)_{ijkl} = \frac{1}{3} g_1(J^e, s) J^{e\frac{2}{3}} \delta_{ij} + \frac{1}{2} g_2(s) \left(F^e_{kl}\delta_{jl} + F^e_{kj}\delta_{il}\right) \tag{43a}$$

$$\left(\frac{\partial \mathbf{F}^e}{\partial \mathbf{F}}\right)_{ijkl} = \delta_{ik} F^{d-1}_{lj} \tag{43b}$$

$$\left(\frac{\partial \mathbf{F}^{e^{-1}}}{\partial \mathbf{F}^e}\right)_{ijkl} = -F^{e^{-1}}_{ik} F^{e^{-1}}_{lj} \tag{43c}$$

Now using Eqs. (24) and (34), $\mathbf{P}$ is given as:

$$\mathbf{P} = \rho_0 \frac{\partial \psi^e}{\partial \mathbf{F}} + \sum_{i=1}^{n} \rho_0 \frac{\partial \psi^I_i}{\partial \mathbf{F}} + \beta_{lu} \mathbf{F}\dot{\mathbf{E}} \tag{44}$$

where

$$\begin{aligned} \rho_0 \frac{\partial \psi^e}{\partial \mathbf{F}} &= \rho_0 \frac{\partial \psi^e}{\partial \tilde{\mathbf{E}}^e} : \frac{\partial \tilde{\mathbf{E}}^e}{\partial \mathbf{F}^e} : \frac{\partial \mathbf{F}^e}{\partial \mathbf{F}} \\ &= \frac{1}{3} g_1(J^e, s) J^{e\frac{2}{3}} \left(\mathbf{I} : \mathbb{C}^e : \tilde{\mathbf{E}}^e\right) \mathbf{F}^{-T} \\ &\quad + g_2(s) \mathbf{F}^e \left(\mathbb{C}^e : \tilde{\mathbf{E}}^e\right) \mathbf{F}^{d-T} \end{aligned} \tag{45}$$

and

$$\begin{aligned} \rho_0 \frac{\partial \psi^I_i}{\partial \mathbf{F}} &= \gamma_{l_I} \frac{\partial \phi_i}{\partial \mathbf{F}} \\ &= \gamma_{l_I} \left(\frac{\partial \phi_i}{\partial \Delta_{Ni}} \frac{\partial \Delta_{Ni}}{\partial \mathbf{F}} + \frac{\partial \phi_i}{\partial \Delta_{Ti}} \frac{\partial \Delta_{Ni}}{\partial \mathbf{F}}\right) \\ &= \gamma_{l_I} \left(T_n \frac{\partial \Delta_{Ni}}{\partial \mathbf{F}^e} : \frac{\partial \mathbf{F}^e}{\partial \mathbf{F}} + T_t \frac{\partial \Delta_{Ni}}{\partial \mathbf{F}^e} : \frac{\partial \mathbf{F}^e}{\partial \mathbf{F}}\right) \end{aligned} \tag{46}$$

in which T_n and T_t are computed from Eq. (28) and $\frac{\partial \Delta_N}{\partial \mathbf{F}^e}$ and $\frac{\partial \Delta_N}{\partial \mathbf{F}^e}$ can be derived as:

$$\frac{\partial \Delta_{Ni}}{\partial \mathbf{F}^e} = -h \mathbf{N}^I_i \otimes \mathbf{N}^I_i : \frac{\partial \mathbf{F}^{e^{-1}}}{\partial \mathbf{F}^e} \tag{47a}$$

$$\frac{\partial \Delta_{Ti}}{\partial \mathbf{F}^e} = -\frac{h}{\Delta_{Ti}} \left(\mathbf{J}_i \otimes \mathbf{N}^I_i + \Delta_{Ni} \mathbf{N}^I_i \otimes \mathbf{N}^I_i\right) : \frac{\partial \mathbf{F}^{e^{-1}}}{\partial \mathbf{F}^e} \tag{47b}$$

Appendix C: Stored elastic energy density for small deformation kinematics

The stored elastic energy density in Eq. (6) takes the following form for an isotropic material under small strain conditions i.e. ($\mathbf{F}^e \approx \mathbf{I}$) [74]:

$$\rho_0 \psi^e = (1-s)^2 \left[\frac{K}{2} \langle \mathrm{tr}\left(\boldsymbol{\epsilon}^e\right)\rangle_+^2 + \mu \mathrm{tr}\left(\boldsymbol{\epsilon}^{e^2}_{dev}\right)\right] + \frac{K}{2} \langle \mathrm{tr}\left(\boldsymbol{\epsilon}^e\right)\rangle_-^2 \tag{48}$$

where $\boldsymbol{\epsilon}^e$ and $\boldsymbol{\epsilon}^e_{dev}$ represent the linear elastic strain tensor and its deviatoric component respectively. K and μ are the bulk and shear modulus respectively.

The linear elastic strain tensor in the presence of interfaces is given as [60,85]:

$$\boldsymbol{\epsilon}^e = \nabla^{sym} \mathbf{u} - \sum_{i=1}^{n} [\![\mathbf{u}]\!]_i \otimes^{sym} \mathbf{N}^I_i \gamma_{l_I} \tag{49}$$

where ∇^{sym} is the symmetric gradient operator and $\otimes^{sym}$ represents the symmetric tensor product.

References

1. Abdollahi A, Arias I (2012) Phase-field modeling of crack propagation in piezoelectric and ferroelectric materials with different electromechanical crack conditions. J Mech Phys Solids 60(12):2100–2126
2. Abedi R, Hawker MA, Haber RB, Matous K (2010) An adaptive spacetime discontinuous Galerkin method for cohesive models of elastodynamic fracture. Int J Numer Methods Eng 81(10):1207–1241
3. Aldakheel F, Hudobivnik B, Hussein A, Wriggers P (2018) Phase-field modeling of brittle fracture using an efficient virtual element scheme. Comput Methods Appl Mech Eng 341:443–466
4. Aldakheel F, Noii N, Wick T, Wriggers P (2020) A global-local approach for hydraulic phase-field fracture in poroelastic media. arXiv:2001.06055
5. Ambati M, Gerasimov T, De Lorenzis L (2015a) A review on phase-field models of brittle fracture and a new fast hybrid formulation. Comput Mech 55(2):383–405
6. Ambati M, Gerasimov T, De Lorenzis L (2015b) Phase-field modeling of ductile fracture. Comput Mech 55(5):1017–1040

7. Ambati M, Kruse R, De Lorenzis L (2016) A phase-field model for ductile fracture at finite strains and its experimental verification. Comput Mech 57(1):149–167
8. Armero F, Garikipati K (1996) An analysis of strong discontinuities in multiplicative finite strain plasticity and their relation with the numerical simulation of strain localization in solids. Int J Solids Struct 33(20–22):2863–2885
9. Ayyagari RS, Daphalapurkar NP, Ramesh KT (2018) The effective compliance of spatially evolving planar wing-cracks. J Mech Phys Solids 111:503–529
10. Babuška I, Banerjee U, Osborn JE (2004) Generalized finite element methods: main ideas, results, and perspective. Int J Comput Methods 1:67–103
11. Belytschko T, Black T (1999) Elastic crack growth in finite elements with minimal remeshing. Int J Numer Methods Eng 45(5):601–620
12. Belytschko T, Gracie R, Ventura G (2009) A review of extended/generalized finite element methods for material modeling. Model Simul Mater Sci Eng 17(4):43001
13. Biner SB, Hu SY (2009) Simulation of damage evolution in composites: a phase-field model. Acta Mater 57(7):2088–2097
14. Black T, Belytschko T (1999) A finite element method for crack growth without remeshing. Int J Numer Methods Eng 45:601–620
15. Borden MJ (2012) Isogeometric analysis of phase-field models for dynamic brittle and ductile fracture. Ph.D. thesis, UT Austin
16. Borden MJ, Verhoosel CV, Scott MA, Hughes TJ, Landis CM (2012) A phase-field description of dynamic brittle fracture. Comput Methods Appl Mech Eng 217–220:77–95
17. Borden MJ, Hughes TJ, Landis CM, Verhoosel CV (2014) A higher-order phase-field model for brittle fracture: formulation and analysis within the isogeometric analysis framework. Comput Methods Appl Mech Eng 273:100–118
18. Bouhala L, Shao Q, Koutsawa Y, Younes A, Núñez P, Makradi A, Belouettar S (2013) An XFEM crack-tip enrichment for a crack terminating at a bi-material interface. Eng Fract Mech 102:51–64
19. Bourdin B, Francfort GA, Marigo JJ (2000) Numerical experiments in revisited brittle fracture. J Mech Phys Solids 48(4):797–826
20. Cheng J, Tu X, Ghosh S (2020) Wavelet-enriched adaptive hierarchical FE model for coupled crystal plasticity-phase field modeling of crack propagation in polycrystalline microstructures. Comput Methods Appl Mech Eng 361:112757
21. Clayton JD, Knap J (2015) Phase field modeling of directional fracture in anisotropic polycrystals. Comput Mater Sci 98:158–169
22. Dittmann M, Aldakheel F, Schulte J, Wriggers P, Hesch C (2018) Variational phase-field formulation of non-linear ductile fracture. Comput Methods Appl Mech Eng 342:71–94
23. Dittmann M, Aldakheel F, Schulte J, Schmidt F, Krüger M, Wriggers P, Hesch C (2020) Phase-field modeling of porous-ductile fracture in non-linear thermo-elasto-plastic solids. Comput Methods Appl Mech Eng 361:112730
24. Francfort GA, Marigo JJ (1998) Revisiting brittle fracture as an energy minimization problem. J Mech Phys Solids 46(8):1319–1342
25. Freed Y, Banks-Sills L (2008) A new cohesive zone model for mixed mode interface fracture in bimaterials. Eng Fract Mech 75(15):4583–4593
26. Fries TP, Belytschko T (2010) The extended/generalized finite element method: an overview of the method and its applications. Int J Numer Methods Eng 84:253–304
27. Gao Y, Bower A (2004) A simple technique for avoiding convergence problems in finite element simulations of crack nucleation and growth on cohesive interfaces. Model Simul Mater Sci Eng 12(3):453
28. Ghaffari Motlagh Y, de Borst R (2020) Considerations on a phase-field model for adhesive fracture. Int J Numer Methods Eng 121(13):2946–2963
29. Gu Y, Jung J, Yang Q, Chen W (2015) An inertia-based stabilizing method for quasi-static simulation of unstable crack initiation and propagation. J Appl Mech 82(10):101010
30. Guillén-Hernández T, García IG, Reinoso J, Paggi M (2019) A micromechanical analysis of inter-fiber failure in long reinforced composites based on the phase field approach of fracture combined with the cohesive zone model. Int J Fract 220:181–203
31. Hansen-Dörr AC, de Borst R, Hennig P, Kästner M (2019) Phase-field modelling of interface failure in brittle materials. Comput Methods Appl Mech Eng 346:25–42
32. Hansen-Dörr AC, Dammaß F, de Borst R, Kästner M (2020) Phase-field modeling of crack branching and deflection in heterogeneous media. Eng Fract Mech 232:107004
33. Hofacker M, Miehe C (2013) A phase field model of dynamic fracture: robust field updates for the analysis of complex crack patterns. Int J Numer Methods Eng 93(3):276–301
34. Jain JR, Ghosh S (2008) Damage evolution in composites with a homogenization-based continuum damage mechanics model. Int J Damage Mech 18(6):533–568
35. Jin ZH, Sun CT (2005) Cohesive zone modeling of interface fracture in elastic bi-materials. Eng Fract Mech 72(12 SPEC. ISS.):1805–1817
36. Karma A, Kessler DA, Levine H (2001) Phase-field model of mode III dynamic fracture. Phys Rev Lett 87:045501
37. Krüger M, Dittmann M, Aldakheel F, Härtel A, Wriggers P, Hesch C (2020) Porous-ductile fracture in thermo-elasto-plastic solids with contact applications. Comput Mech 65(4):941–966
38. Labanda NA, Giusti SM, Luccioni BM (2016) Meso-scale fracture simulation using an augmented Lagrangian approach. Int J Damage Mech 27(1):138–175
39. Leguillon D, Lacroix C, Martin E (2000) Interface debonding ahead of a primary crack. J Mech Phys Solids 48(10):2137–2161
40. Li S, Thouless MD, Waas AM, Schroeder JA, Zavattieri PD (2005) Use of a cohesive-zone model to analyze the fracture of a fiber-reinforced polymer-matrix composite. Compos Sci Technol 65(3–4):537–549
41. Li Z, Ghosh S, Getinet N, O'Brien DJ (2016) Micromechanical modeling and characterization of damage evolution in glass fiber epoxy matrix composites. Mech Mater 99:37–52
42. Liu W, Schesser D, Yang Q, Ling D (2015) A consistency-check based algorithm for element condensation in augmented finite element methods for fracture analysis. Eng Fract Mech 139:78–97
43. Lo YS, Borden MJ, Ravi-Chandar K, Landis CM (2019) A phase-field model for fatigue crack growth. J Mech Phys Solids 132:103684
44. Marigo JJ, Maurini C, Pham K (2016) An overview of the modelling of fracture by gradient damage models. Meccanica 51(12):3107–3128
45. Martin E, Leguillon D, Lacroix C (2001) A revisited criterion for crack deflection at an interface in a brittle bimaterial. Compos Sci Technol 61(12):1671–1679
46. Martínez D, Gupta V (1994) Energy criterion for crack deflection at an interface between two orthotropic media. J Mech Phys Solids 42(8):1247–1271
47. May S, Vignollet J, De Borst R (2015) A numerical assessment of phase-field models for brittle and cohesive fracture: Γ-convergence and stress oscillations. Eur J Mech A Solids 52:72–84
48. May S, Vignollet J, de Borst R (2016) A new arc-length control method based on the rates of the internal and the dissipated energy. Eng Comput 33:100–115
49. Mesgarnejad A, Imanian A, Karma A (2019) Phase-field models for fatigue crack growth. Theor Appl Fract Mech 103:102282
50. Miehe C, Hofacker M, Welschinger F (2010a) A phase field model for rate-independent crack propagation: robust algorithmic implementation based on operator splits. Comput Methods Appl Mech Eng 199(45–48):2765–2778

51. Miehe C, Welschinger F, Hofacker M (2010b) A phase field model of electromechanical fracture. J Mech Phys Solids 58(10):1716–1740
52. Miehe C, Welschinger F, Hofacker M (2010c) Thermodynamically consistent phase-field models of fracture: variational principles and multi-field FE implementations. Int J Numer Methods Eng 83(10):1273–1311
53. Miehe C, Schänzel LM, Ulmer H (2015) Phase field modeling of fracture in multi-physics problems. Part I. Balance of crack surface and failure criteria for brittle crack propagation in thermo-elastic solids. Comput Methods Appl Mech Eng 294:449–485
54. Miehe C, Aldakheel F, Raina A (2016) Phase field modeling of ductile fracture at finite strains: a variational gradient-extended plasticity-damage theory. Int J Plast 84:1–32
55. Ming-Yuan H, Hutchinson JW (1989) Crack deflection at an interface between dissimilar elastic materials. Int J Solids Struct 25(9):1053–1067
56. Moës N, Dolbow J, Belytschko T (1999) A finite element method for crack growth without remeshing. Int J Numer Methods Eng 46(1):131–150
57. Mosler J (2006) Modeling strong discontinuities at finite strains—a novel numerical implementation. Comput Methods Appl Mech Eng 195(33–36):4396–4419
58. Needleman A (1987) A continuum model for void nucleation by inclusion debonding. J Appl Mech 54(3):525–531
59. Needleman A (1992) Micromechanical modelling of interfacial decohesion. Ultramicroscopy 40(3):203–214
60. Nguyen TT, Yvonnet J, Zhu QZ, Bornert M, Chateau C (2016) A phase-field method for computational modeling of interfacial damage interacting with crack propagation in realistic microstructures obtained by microtomography. Comput Methods Appl Mech Eng 312:567–595
61. Nguyen TT, Waldmann D, Bui TQ (2019a) Role of interfacial transition zone in phase field modeling of fracture in layered heterogeneous structures. J Comput Phys 386:585–610
62. Nguyen TT, Yvonnet J, Waldmann D, He QC (2019b) Phase field modeling of interfacial damage in heterogeneous media with stiff and soft interphases. Eng Fract Mech 218:106574
63. Nguyen VP, Nguyen GD, Nguyen CT, Shen L, Dias-da Costa D, El-Zein A, Maggi F (2017) Modelling complex cracks with finite elements: a kinematically enriched constitutive model. Int J Fract 203(1):21–39
64. Noii N, Aldakheel F, Wick T, Wriggers P (2020) An adaptive global-local approach for phase-field modeling of anisotropic brittle fracture. Comput Methods Appl Mech Eng 361:112744
65. Ortiz M, Pandolfi A (1999) Finite-deformation irreversible cohesive elements for three-dimensional crack-propagation analysis. Int J Numer Methods Eng 44(9):1267–1282
66. Paggi M, Reinoso J (2017) Revisiting the problem of a crack impinging on an interface: a modeling framework for the interaction between the phase field approach for brittle fracture and the interface cohesive zone model. Comput Methods Appl Mech Eng 321:145–172
67. París F, Correa E, Mantič V (2006) Kinking of transversal interface cracks between fiber and matrix. J Appl Mech 74(4):703–716
68. Park K, Paulino GH (2011) Cohesive zone models: a critical review of traction-separation relationships across fracture surfaces. Appl Mech Rev 64:060802-1
69. Park K, Paulino GH (2013) Cohesive Zone Models: A Critical Review of Traction-Separation Relationships Across Fracture Surfaces. Appl Mech Rev 64(6):060802
70. Park K, Paulino GH, Roesler JR (2009) A unified potential-based cohesive model of mixed-mode fracture. J Mech Phys Solids 57(6):891–908
71. Patil RU, Mishra BK, Singh IV (2017) A new multiscale XFEM for the elastic properties evaluation of heterogeneous materials. Int J Mech Sci 122:277–287
72. Pham K, Amor H, Marigo JJ, Maurini C (2010) Gradient damage models and their use to approximate brittle fracture. Int J Damage Mech 20(4):618–652
73. Schneider D, Schoof E, Huang Y, Selzer M, Nestler B (2016) Phase-field modeling of crack propagation in multiphase systems. Comput Methods Appl Mech Eng 312:186–195
74. Shahba A, Ghosh S (2019) Coupled phase field finite element model for crack propagation in elastic polycrystalline microstructures. Int J Fract 219(1):31–64
75. Silling SA (2000) Reformulation of elasticity theory for discontinuities and long-range forces. J Mech Phys Solids 48:175–209
76. Silling SA, Weckner O, Askari E, Bobaru F (2010) Crack nucleation in a peridynamic solid. Int J Fract 162(1–2):219–227
77. Simo JC, Oliver J, Armero F (1993) An analysis of strong discontinuities induced by strain-softening in rate-independent inelastic solids. Comput Mech 12(5):277–296
78. Singh N, Verhoosel C, De Borst R, Van Brummelen E (2016) A fracture-controlled path-following technique for phase-field modeling of brittle fracture. Finite Elem Anal Des 113:14–29
79. Song L, Meng S, Xu C, Fang G, Yang Q (2019) Finite element-based phase-field simulation of interfacial damage in unidirectional composite under transverse tension. Model Simul Mater Sci Eng 27(5):55011
80. Spring DW, Paulino GH (2014) A growing library of three-dimensional cohesive elements for use in ABAQUS. Eng Fract Mech 126:190–216
81. Tu X, Ray A, Ghosh S (2020) A coupled crystal plasticity FEM and phase-field model for crack evolution in microstructures of 7000 series aluminum alloys. Eng Fract Mech 230:106970
82. Verhoosel CV, de Borst R (2013) A phase-field model for cohesive fracture. Int J Numer Methods Eng 96(1):43–62
83. Wang Y, Waisman H (2017) Material-dependent crack-tip enrichment functions in XFEM for modeling interfacial cracks in bimaterials. Int J Numer Methods Eng 112(11):1495–1518
84. Wilson ZA, Landis CM (2016) Phase-field modeling of hydraulic fracture. J Mech Phys Solids 96:264–290
85. Xia L, Yvonnet J, Ghabezloo S (2017) Phase field modeling of hydraulic fracturing with interfacial damage in highly heterogeneous fluid-saturated porous media. Eng Fract Mech 186:158–180
86. Xu XP, Needleman A (1993) Void nucleation by inclusion debonding in a crystal matrix. Modell Simul Mater Sci Eng 1:111
87. Xu XP, Needleman A (1994) Numerical simulations of fast crack growth in brittle solids. J Mech Phys Solids 42(9):1397–1434
88. Zhang P, Hu X, Yang S, Yao W (2019) Modelling progressive failure in multi-phase materials using a phase field method. Eng Fract Mech 209:105–124
89. Zhang P, Feng Y, Bui TQ, Hu X, Yao W (2020) Modelling distinct failure mechanisms in composite materials by a combined phase field method. Compos Struct 232:111551
90. Zienkiewicz OC, Taylor RL, Sherwin SJ, Peiro J (2003) On discontinuous Galerkin methods. Int J Numer Methods Eng 58(8):1119–1148